

Chapter 6

Alloy Oxidation II: Internal Oxidation

6.1 INTRODUCTION

As recognised in Chapter 5, when an alloy component is selectively oxidised but cannot reach the surface quickly enough to develop a scale, then internal oxidation results. Furthermore, an alloy which initially contains a sufficient amount of the reacting metal to form a scale can become depleted in that component to the extent that internal oxidation commences. Under some circumstances, internal oxidation and external scaling can occur simultaneously. The practical reality [1] is that a large percentage of high-temperature corrosion failures involve internal oxidation. It is therefore important to establish more precisely the conditions under which this mode of attack occurs, the rate of the process and how it varies with alloy composition and ambient conditions.

The general features of internal oxidation reactions were first established by Smith [2,3], Rhines et al. [4,5] and Meijering and Druyvesten [6,7]. Many subsequent investigations have added to our descriptive knowledge of the process. We consider first some experimental results, with the aim of relating reaction morphologies to the phase diagrams which describe the phase assemblages encountered. The conditions under which these morphologies develop are then established, and the kinetics described using Wagner's diffusion analysis [8] and its explication by Rapp [9]. These descriptions are then extended to other, more complex situations, where the simplifying assumptions adopted by Wagner are no longer applicable. It is emphasised that 'oxidation' means forming a compound (oxide, carbide, nitride, etc.) of the reactive alloy solute metal, and the description given here applies to internal oxidation, carburisation, nitridation, etc.

6.2 SELECTED EXPERIMENTAL RESULTS

Typical reaction morphologies of internally oxidised alloys are shown in Fig. 6.1, where chromium-rich oxide has precipitated inside an Fe-5Cr alloy reacted under conditions where the ambient p_{O_2} value was too low for FeO to

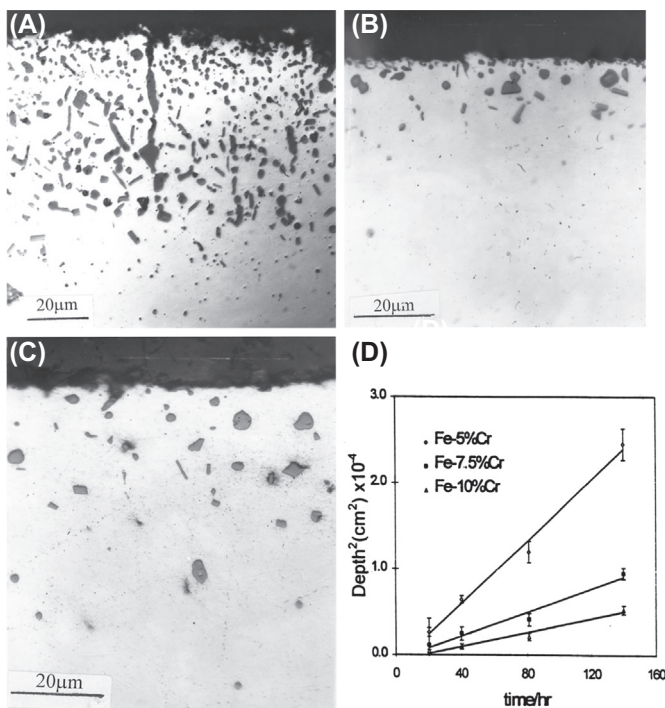


FIGURE 6.1 Internal oxidation of Fe-5Cr at $p_{O_2} = 8.7 \times 10^{-17}$ atm: (A) 900°C; (B) 1000°C; (C) 1100°C; (D) internal oxidation kinetics at 1000°C. Reproduced from O. Ahmed, D.J. Young, in: M.J. McNallan, E.J. Opila, T. Maruyama, T. Narita (Eds.), *High Temperature Corrosion and Materials Chemistry II*, The Electrochemical Society, Inc., Pennington, NJ (2000), 77, by permission of The Electrochemical Society.

form. Clearly oxygen had dissolved in the alloy and diffused inwards to react with alloy solute chromium, precipitating its oxide. The depth of the precipitation zone, $X_{(i)}$, is seen in Fig. 6.1 to increase according to parabolic kinetics

$$X_{(i)}^2 = 2k_p^{(i)} t \quad [6.1]$$

where $k_p^{(i)}$ is the internal oxidation rate constant. This is an almost universal observation [11,12] and indicates that the process is diffusion controlled.

The effect of alloy chromium content is shown in Fig. 6.2. Dilute alloys form only internal oxide, Fe-10Cr forms both external and internal oxide and Fe-17Cr forms only an external scale. A schematic phase diagram in Fig. 6.3 illustrates diffusion paths corresponding to the steady-state morphologies of Figs 6.2A–D. The diagram has been constructed on the basis that p_{O_2} is too low for any iron-bearing oxide, such as $FeCr_2O_4$, to form. Thus pure iron equilibrates directly with oxygen. Paths (a) and (b) show variation in oxygen

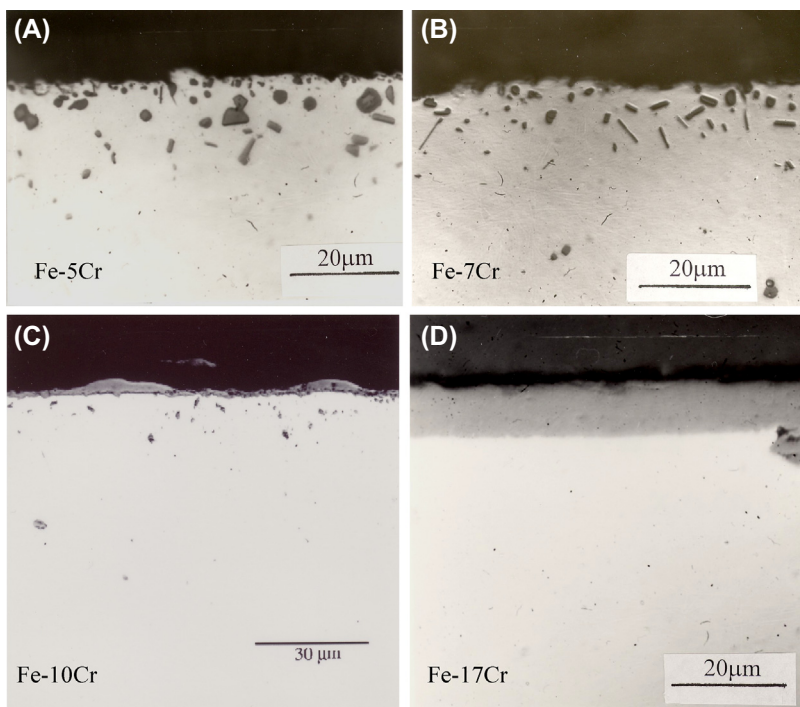


FIGURE 6.2 Change in oxide morphology with composition of Fe-Cr alloys exposed to $p_{O_2} = 8.7 \times 10^{-17}$ atm at 1000°C. (A) Fe-5Cr; (B) Fe-7Cr; (C) Fe-10Cr; (D) Fe-17Cr. Reproduced from O. Ahmed, D.J. Young, in: M.J. McNallan, E.J. Opila, T. Maruyama, T. Narita (Eds.), *High Temperature Corrosion and Materials Chemistry II*, The Electrochemical Society, Inc., Pennington, NJ (2000), 77, by permission of The Electrochemical Society.

content at a fixed N_{Cr}/N_{Fe} ratio and correspond to the situation $D_o \gg D_{AB}$, where oxygen diffuses into the alloy so fast that chromium diffusion can be neglected. These paths represent local equilibrium situations and do not encompass the supersaturation zones necessary to drive precipitate nucleation (Section 6.7). Path (c) represents simultaneous internal and external oxidation, and path (d) shows external scaling only.

The chromium oxide precipitates shown in Figs 6.1 and 6.2 are dispersed and are generally spheroidal in shape, although nonuniform in size. Moreover, the volume fraction of precipitate appears to vary somewhat with depth at higher temperatures, although it is approximately constant at 900°C. A very different precipitate shape is obtained by internal nitridation, as seen in Fig. 6.4. Lamellar precipitates of Cr₂N have grown into the alloy, aligned approximately normal to the sample surface, ie, in a direction parallel to that in which the reaction is proceeding. Clearly the competition between precipitate nucleation and growth has led to very different outcomes in the oxidation and nitridation reactions.

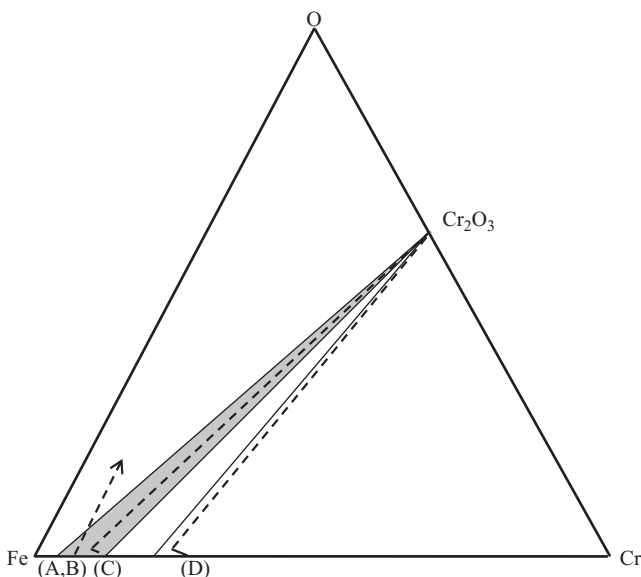


FIGURE 6.3 Schematic phase diagram for Fe-Cr-O with Cr₂O₃ as the only stable oxide. Diffusion paths (A) to (D) correspond to the reaction morphologies in Fig. 6.2A–D.

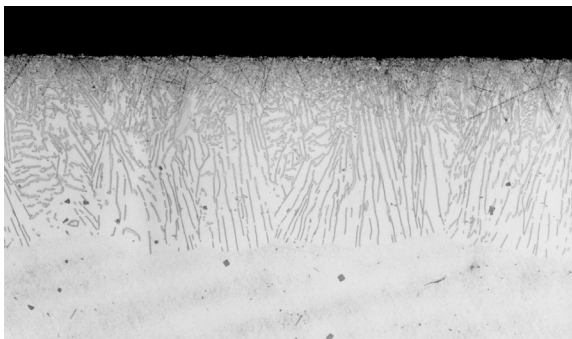


FIGURE 6.4 Optical micrograph of lamellar Cr₂N precipitates formed in Fe-20Ni-25Cr reacted at 1000°C with N₂-10%H₂.

It was observed in Chapter 5 that cold working an alloy surface by grinding introduced subsurface defects which accelerated alloy diffusion, making external scale formation by the selectively oxidised component more likely at moderate temperatures. As seen in Fig. 6.5, Incoloy 617 forms a protective Cr₂O₃ scale when surface ground before reaction. However, when the deformed region is removed by chemical polishing, both internal and external oxidation develop during subsequent reactions. Of further interest is the finding that internal oxidation occurred preferentially at grain boundaries,

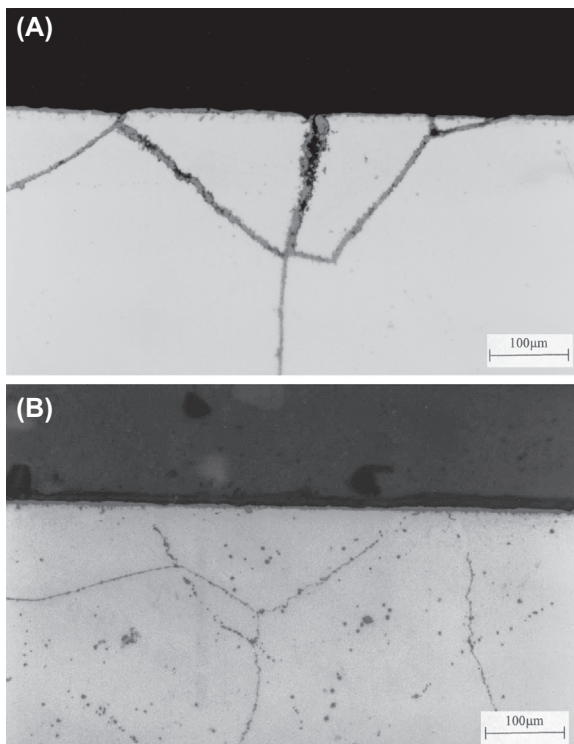


FIGURE 6.5 Oxidation of IN 617 at $T = 700^\circ\text{C}$, $p_{\text{O}_2} = 1 \times 10^{-23}$ atm. (A) Grain boundary precipitation of Cr_2O_3 in material prepared by chemical polishing. (B) External Cr_2O_3 scale on material prepared by surface grinding.

rather than within the grains. Penetration along the grain boundaries involved oxidation of alloy carbides and was remarkably fast. It turns out that internal oxidation at grain boundaries is common in austenitic alloys.

In a number of alloys, the selectively reacted component can form more than one product phase. A frequently encountered example is the precipitation of chromium-rich carbides during carburisation of heat-resisting alloys. Fig. 6.6 shows a cross-section of carburised Fe-37.5Ni-25Cr, where two precipitation zones have been revealed by their different response to stain etching. The carbides in the near surface zone are chromium-rich M_7C_3 , and those in the deeper zone are chromium-rich M_{23}C_6 . Carburisation reactions are discussed more fully in Chapter 9.

As already indicated, diverse precipitate morphologies are possible. Further examples are shown in Fig. 6.7. Strongly directional growth of alumina precipitates in the diffusion direction has occurred, Widmanstätten plates of Cr_2N have developed and apparently lamellar, chromium-rich M_{23}C_6 has grown into an Fe-25Cr alloy. Questions of interest concern the factors

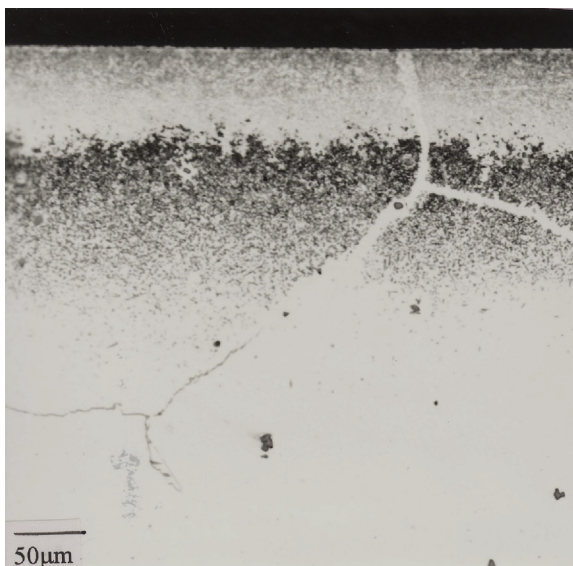


FIGURE 6.6 Internal carburisation of Fe-37.5Ni-25Cr at 1000°C in gas with $a_C = 1$: near surface zone contains Cr_7C_3 precipitates, deeper zone contains Cr_{23}C_6 (etched with Murakami's reagent).

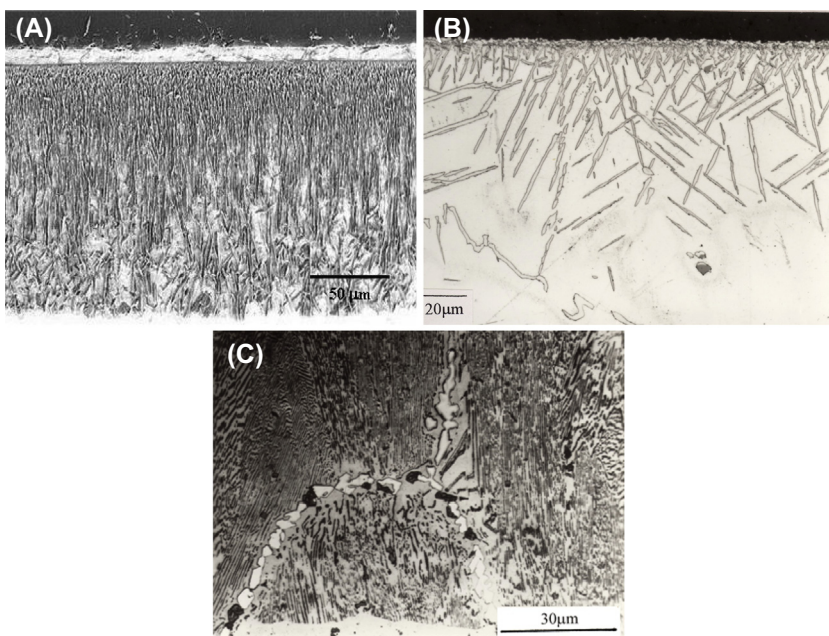


FIGURE 6.7 Diverse precipitate morphologies resulting from internal oxidation reactions. (A) Oxidation of Ni-2.5Al at $T = 1000^\circ\text{C}$, $p_{\text{O}_2} = 4.6 \times 10^{-11}$ atm. (B) Nitridation of Ni-15Fe-25Cr in $\text{N}_2\text{-}10\%\text{H}_2$ at 1000°C. (C) Carburisation of Fe-17Cr at 1000°C in gas with $a_C = 1$, showing internal reaction front.

controlling the predominance of precipitate growth over nucleation, what controls the orientation of the precipitate with respect to the metal matrix and the diffusion direction, and whether or not the aligned precipitate-matrix interfaces can provide preferred diffusion pathways for the oxidant, thereby accelerating the corrosion rate.

Alloys can contain more than one component capable of internally precipitating an oxide. Oxidation of a model alloy Ni-3.5Cr-2.5Al led to the internal precipitation of both chromium and aluminium-rich oxides, as shown in Fig. 6.8, a cross-sectional image obtained by SEM. The image brightness is related to the average atomic number of the material being imaged. Thus the metal matrix, which is mainly nickel, is bright, the chromium-rich oxide is grey and the aluminium-rich oxide appears dark. Clearly the more stable aluminium-rich oxide is precipitated to greater depth than the chromium-rich oxide. This reflects the gradient in oxygen activity from its maximum at the alloy surface to a minimum in the alloy interior.

The conditions under which internal oxidation is possible can be specified in a general way and are formulated here for a binary alloy AB. Internal precipitation of BO_v can occur if this oxide is more stable than that of metal A per mole of oxygen. Precipitation will occur if oxygen can dissolve in the alloy and diffuse inward so as to achieve an activity high enough to stabilise BO_v , but not AO. The precipitates will be distributed internally rather than aggregating to form a scale if N_B is sufficiently low. It is desirable to be able to specify the critical value of N_B separating these two regimes of oxidation. As always, we wish to predict the rate of the process and how it varies with material properties and environmental factors.

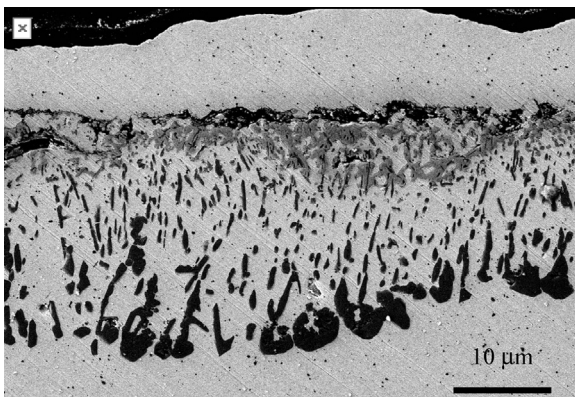


FIGURE 6.8 Simultaneous internal oxidation of chromium and aluminium in Ni-3.5Cr-2.5Al at $T = 1000^\circ\text{C}$, $p_{\text{O}_2} = 9.8 \times 10^{-13}$ atm in Ar-H₂-H₂O. Grey oxide is chromium-rich and dark oxide is aluminium-rich. A pure nickel layer is present at the surface.

As seen from the brief survey of experimental results, a full description of the process also involves predicting precipitate size, shape, orientation and distribution. The kinetics of internal oxidation are considered first, and a number of simple limiting cases are identified. The factors affecting precipitate nucleation, growth, morphologies and distributions are then considered. Predictions for the transition between internal and external oxidation are then compared with experimental data. The effects of the volume expansion accompanying internal oxide precipitation are discussed, and finally, effects of water vapour on internal oxidation are briefly examined.

6.3 INTERNAL OXIDATION KINETICS IN THE ABSENCE OF EXTERNAL SCALING

We consider an alloy AB exposed to an oxygen potential high enough to react with B, but not with A, and suppose that alloy diffusion is negligible compared with inward oxygen movement. Internal oxidation will result if the oxygen solubility in the B-depleted alloy, $N_o^{(s)}$, and its diffusion coefficient, D_o , are high enough. If, furthermore, the precipitate BO_v is extremely stable, then the reaction zone is assumed to consist of precipitates embedded in a matrix of almost pure A. This assumption is based on the thermodynamics of the reaction



discussed in Section 2.4. The solubility product for local equilibrium between precipitate and matrix

$$N_B N_o^v = K_{sp} = \exp(-\Delta G^P / RT) \quad [6.3]$$

with

$$\Delta G^P = \Delta G_f^\circ(\text{BO}_v) - \Delta \bar{G}_B - v \Delta \bar{G}_O \quad [6.4]$$

is very small for a high stability precipitate. Although it is not necessarily so, it was originally assumed [8,9] that both N_B and N_o are very low throughout the precipitation zone, as represented in Fig. 6.9. Thus oxygen diffuses through a metal matrix of almost pure A, between the BO_v precipitates which have already formed, to reach the reaction front at a depth $X^{(i)}$, where more B is available for reaction. An approximate estimate of the internal penetration rate can be made from a mass balance at the reaction front.

Reformulating the standard expression (Eq. [5.29]) for mass balance at a moving boundary in terms appropriate to the development of a two-phase zone, we can write

$$J_o^{\text{ioz}} - J_o^{\text{all}} = u(C_o^{\text{ioz}} - C_o^{\text{all}}) \quad [6.5]$$

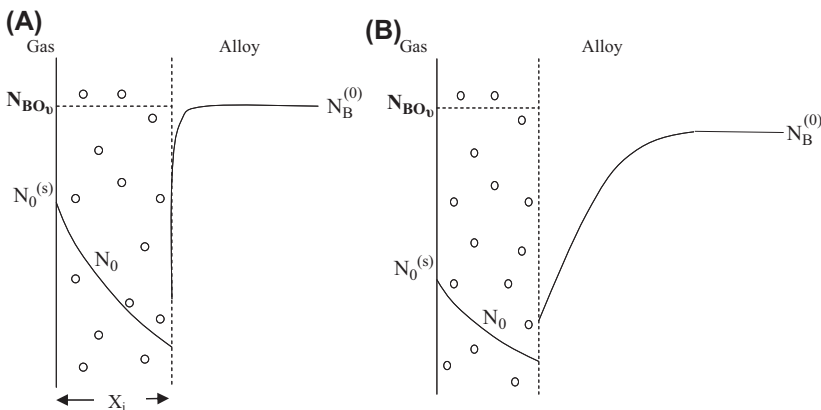


FIGURE 6.9 Schematic representation of internal precipitation of a very stable oxide and the reactant concentration profiles: (A) component B almost immobile and (B) both oxygen and B diffuse.

where the superscripts iox and all refer to the internal oxidation zone and the base alloy, and C_o^{iox} represents the overall oxygen concentration in the oxide plus matrix two-phase region. Given the assumption that the oxygen concentration at the reaction front is zero, it follows that

$$C_o^{\text{all}} = o = J_o^{\text{all}} \quad [6.6]$$

Approximating further that the oxygen flux

$$J_o^{\text{iox}} = -D_o \frac{\partial C_o}{\partial x} \approx D_o \frac{C_o^{(s)} - C_o^{(X)}}{X_{(i)}} \quad [6.7]$$

setting $C_o^{(X)} = 0$ (Fig. 6.9) and substituting Eq. [6.7] in Eq. [6.5] yields

$$\frac{D_o C_o^{(s)}}{X_{(i)}} = \frac{dX_{(i)}}{dt} C_o^{\text{iox}} \quad [6.8]$$

Integration of Eq. [6.8] and substitution from the stoichiometric relationship

$$C_o^{\text{iox}} = v C_B^{(o)} \quad [6.9]$$

with $C_B^{(o)}$ the original alloy concentration of B, then leads to Eq. [6.1], with

$$k_p^{(i)} = \frac{D_o C_o^{(s)}}{v C_B^{(o)}} \quad [6.10]$$

It is usually assumed that the molar volumes of the alloy and the matrix A are the same, and hence

$$k_p^{(i)} = \frac{D_o N_o^{(s)}}{v N_B^{(o)}} \quad [6.11]$$

This simple result is intuitively reasonable in that it reflects the fact that the penetration rate is proportional to oxygen permeability, $N_o^{(s)} D_o$, and inversely proportional to the concentration of reactant metal. It should be noted that it has been assumed that the oxide precipitates do not interfere with inward oxygen diffusion.

A more rigorous and less restrictive analysis has been provided by Wagner [8,9], allowing for the possibility that component B also diffuses. The diffusion model is shown schematically in Fig. 6.9B. Again it is assumed that K_{sp} is extremely small, and that both N_o and N_B are vanishingly small at the reaction front. The problem then is to solve the diffusion equations for both B and O:

$$\frac{\partial N_i}{\partial t} = D \frac{\partial^2 N_i}{\partial x^2} \quad [6.12]$$

for the boundary conditions

$$N_o = N_o^{(s)} \quad \text{for } x = 0, \quad t > 0 \quad [6.13]$$

$$N_o = 0 \quad \text{for } x \geq X_{(i)}, \quad t > 0 \quad [6.14]$$

$$N_B = N_B^{(o)} \quad \text{for } x > 0, \quad t = 0 \quad [6.15]$$

$$N_B = 0 \quad \text{for } x \leq X_{(i)}, \quad t > 0 \quad [6.16]$$

The solutions are

$$N_o = N_o^{(s)} \left\{ 1 - \frac{\operatorname{erf}(x/2\sqrt{D_o t})}{\operatorname{erf}\gamma} \right\} \quad [6.17]$$

$$N_B = N_B^{(o)} \left\{ 1 - \frac{\operatorname{erfc}(x/2\sqrt{D_B t})}{\operatorname{erfc}(\gamma\phi^{\frac{1}{2}})} \right\} \quad [6.18]$$

for parabolic kinetics, where Eq. [6.1] applies, with

$$\gamma = \left(k_p^{(i)} / 2D_o \right)^{\frac{1}{2}} \quad [6.19]$$

and

$$\phi = D_o / D_B \quad [6.20]$$

Wagner dealt with the mass balance at the reaction front ($x = X_{(i)}$) by supposing that all precipitation took place at this location, and therefore the fluxes of O and B towards the interface were equivalent:

$$-D_o \left(\frac{\partial N_o}{\partial x} \right)_{x=X_{(i)}-\varepsilon} = v D_B \left(\frac{\partial N_B}{\partial x} \right)_{x=X_{(i)}+\varepsilon} \quad [6.21]$$

Here ε is a very small increment in x , used to indicate that the fluxes are evaluated very close to, but on opposite sides, of the reaction front. Substitution from Eq. [6.17] and Eq. [6.18] into Eq. [6.21] leads, after differentiation, to

$$\frac{N_o^{(s)}}{N_B^{(o)}} = \frac{\exp(\gamma^2) \operatorname{erf}\gamma}{\phi^{\frac{1}{2}} \exp(\gamma^2 \phi) \operatorname{erfc}(\gamma \phi^{\frac{1}{2}})} \quad [6.22]$$

The quantity γ , and hence k_p , can be evaluated numerically from this equation.

In the special case where

$$\frac{D_B}{D_o} \ll \frac{N_o^{(s)}}{N_B^{(o)}} \ll 1 \quad [6.23]$$

then $\gamma \ll 1$ and $\gamma \phi^{\frac{1}{2}} \gg 1$, and Eq. [6.22] can be accurately approximated by

$$\gamma \approx \left(\frac{N_o^{(s)}}{2vN_B^{(o)}} \right)^{\frac{1}{2}} \quad [6.24]$$

Substitution of this result into Eq. [6.19] then yields the simple result Eq. [6.11]. Inspection of Eq. [6.23] reveals that the required condition amounts to a high oxygen permeability relative to any B diffusion, which was the basis for the derivation of Eq. [6.10], and is represented by Fig. 6.9A. If, on the other hand, diffusion of B is important, another special case can arise if

$$\frac{N_o^{(s)}}{N_B^{(o)}} \ll \frac{D_B}{D_o} \ll 1 \quad [6.25]$$

In this case, $\gamma \ll 1$ and $\gamma \phi^{\frac{1}{2}} \ll 1$, and Eq. [6.22] can be approximated by

$$\gamma \approx \frac{\pi^{\frac{1}{2}} \phi^{\frac{1}{2}} N_o^{(s)}}{2vN_B^{(o)}} \quad [6.26]$$

which, when combined with Eqs [6.19] and [6.20], yields

$$k_p^{(i)} = \frac{\pi}{2D_B} \left(\frac{D_o N_o^{(s)}}{2vN_B^{(o)}} \right)^2 \quad [6.27]$$

This is the situation represented by Fig. 6.9B and corresponds to enrichment of B within the precipitation zone as a result of its rapid diffusion from within the alloy towards the surface.

In distinguishing the two limiting cases represented by Eqs [6.11] and [6.27], it is necessary to evaluate the oxidant permeability $N_o^{(s)} D_o$ and the corresponding alloy quantity, $N_B^{(o)} D_B$. The oxidant solubility is related to the surface oxygen activity via Sievert's Equation (Eq. [2.71]). The maximum value of p_{O_2} possible is that at which component A forms an external scale. Thus, for example, internal oxidation of Fe-Cr is limited to a maximum $N_o^{(s)}$ value given by

$$N_o^{(s)} = K [p_{O_2}(\text{FeO})]^{\frac{1}{2}} \quad [6.28]$$

where K is the Sievert's law constant for O_2 in iron. In order to avoid the complications of scale formation (see Section 6.12), it is common to study internal oxidation by controlling p_{O_2} at the level set by the A/AO equilibrium. This is conveniently done using a 'Rhines pack' [4]: a sealed capsule containing a large quantity of powdered metal A mixed with its lowest oxide, along with the AB alloy sample.

Oxygen solubility data shown in Table 6.1 are calculated from Table 2.2. Its use is based on the supposition that all of the reactive component is precipitated near the alloy surface, and oxygen solubility in the almost pure iron or nickel is set by the Rhines pack condition. Data for both ferritic and austenitic iron are provided, for reasons which are now discussed.

Diffusion in ferritic alloys is complicated at certain temperatures by the appearance of a γ (fcc)-phase. Reference to the phase diagrams for Fe-Cr, Fe-Al and Fe-Si in Fig. 6.10 shows that all alloys, when sufficiently dilute, are

TABLE 6.1 Permeability Data for Internal Oxidation in Rhines Packs

| Alloy | T (°C) | In Matrix A | | In Alloy AB ^a | | $N_o^{(s)} D_o / N_B^{(o)} D_B$ |
|-------|-------------|------------------------------|------------------------------|-------------------------------|-------------|---------------------------------|
| | | $N_o^{(s)}$ | D_o (cm 2 s $^{-1}$) | D_B (cm 2 s $^{-1}$) | $N_B^{(o)}$ | |
| Fe-Cr | 1000 | $4.5 \times 10^{-6}(\alpha)$ | $3.5 \times 10^{-6}(\alpha)$ | | 0.054 | |
| | | $3.3 \times 10^{-6}(\gamma)$ | $7.3 \times 10^{-7}(\gamma)$ | $1.5 \times 10^{-11}(\gamma)$ | | 3.0 |
| Fe-Al | 1000 | $4.5 \times 10^{-6}(\alpha)$ | $3.5 \times 10^{-6}(\alpha)$ | $4.2 \times 10^{-10}(\alpha)$ | 0.020 | 1.9 |
| | | $3.3 \times 10^{-6}(\gamma)$ | $7.3 \times 10^{-7}(\gamma)$ | | | |
| Fe-Si | 1150 | $1.5 \times 10^{-5}(\alpha)$ | $9.3 \times 10^{-6}(\alpha)$ | $6.3 \times 10^{-9}(\alpha)$ | 0.016 | 1.4 |
| | | $9.0 \times 10^{-6}(\gamma)$ | $3.9 \times 10^{-7}(\gamma)$ | | | |
| Ni-Cr | 1000 | 4.8×10^{-4} | 9.1×10^{-9} | 7.2×10^{-12} | 0.056 | 10.8 |
| Ni-Al | 1200 | 9.4×10^{-4} | 7.5×10^{-8} | 1.0×10^{-9} | 0.043 | 1.6 |
| Ni-Si | 1000 | 4.8×10^{-4} | 9.1×10^{-9} | 3.9×10^{-11} | 0.016 | 7 |

^aAlloy compositions chosen to match examples studied experimentally.

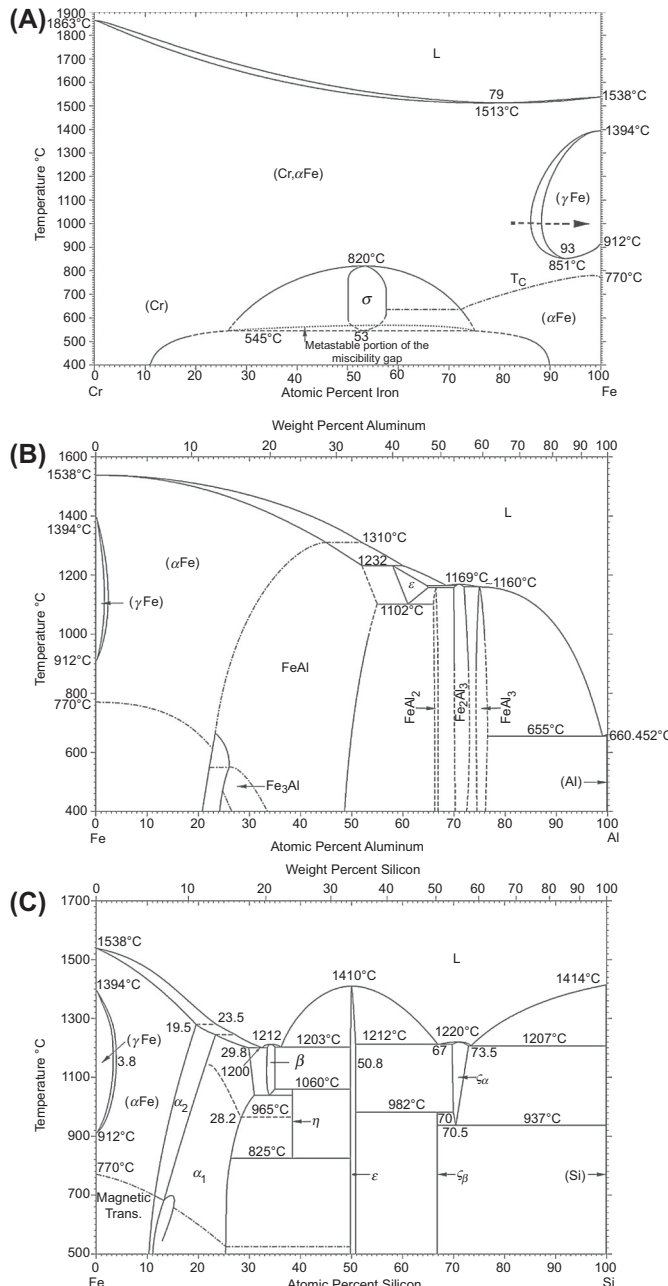


FIGURE 6.10 Phase diagrams for (A) Fe-Cr, (B) Fe-Al and (C) Fe-Si showing γ -phase regions, and diffusion path in metallic part of internally oxidised Fe-Cr (see text).

austenitic at temperatures around 900–1400°C. Consider, for example, an alloy of original composition Fe-15Cr, which at $T = 1000^\circ\text{C}$ is ferritic. Internal oxidation removes most of the chromium from the metal phase, shifting its composition into the γ -region. If the small concentration of dissolved oxygen can be ignored, the diffusion path in the metal region of the reacting alloy is as shown in Fig. 6.10A. For this reason, it is appropriate to consider oxygen dissolution and diffusion through austenite. The $\alpha \rightarrow \gamma$ transformation can be suppressed [13] by the addition of an unreactive ferrite stabiliser such as tin, and data for ferrite are also provided in Table 6.1. Similarly, data for D_B (calculated from data in Appendix D) in both α - and γ -Fe are provided, where available.

It is seen in Table 6.1 that for the conditions chosen, $D_o N_o^{(s)} > D_{\text{Cr}} N_{\text{Cr}}^{(o)}$ and the conditions for Eqs [6.24] and [6.11] are met. Even in the case of much more mobile silicon and aluminium, the conditions are close to being realised, and Eq. [6.11] is expected to provide a reasonable approximation. In this situation, the internal oxidation process is controlled by inward oxygen diffusion, and counterdiffusion of the alloy solute metal can be ignored. If, however, counterdiffusion of the reacting metal is important, then it will enrich in the internal oxidation zone as additional oxide precipitates. Such a situation can be expected during oxidation at very low p_{O_2} values, when the oxygen permeability is consequently lowered.

Wagner [8] also calculated the degree of solute enrichment in the precipitation zone. Defining f_{BO} as the mole fraction of BO_v precipitate in the internal oxide zone, an enrichment factor

$$\alpha = \frac{f_{\text{BO}}}{N_B^{(o)}} \quad [6.29]$$

is identified, and was evaluated by Wagner as

$$\alpha = \left[\pi^{\frac{1}{2}} u \exp(u^2) \operatorname{erfc} u \right]^{-1} \quad [6.30]$$

with $u = \gamma\phi^{\frac{1}{2}}$. Under the limiting conditions of Eq. [6.25], this result can be approximated as

$$\alpha = \left(\pi^{\frac{1}{2}} u \right)^{-1} = \frac{2v N_B^{(o)} D_B}{\pi N_o^{(s)} D_o} \quad [6.31]$$

6.4 EXPERIMENTAL VERIFICATION OF DIFFUSION MODEL

As already mentioned, internal oxidation almost invariably follows parabolic kinetics. The applicability of the simple form Eq. [6.11] is first investigated. One obvious and useful prediction from this equation is that for a given solvent A, the rate of internal oxidation is independent of the chemical identity of B

and is determined solely by the permeability of oxygen in A, together with the oxide stoichiometry. If correct, this provides a method for measuring oxygen permeability. Alloys based on silver provide a good test of this possibility, because Ag_2O is unstable at high temperatures, and reliable independent measurements of $N_o^{(s)}$ and D_o are available [14].

Values of $D_o N_o^{(s)}$ derived from measurements of X_i as a function of time (Eqs [6.1] and [6.11]) have been collected by Meijering [11] and are compared in Fig. 6.11 with independent permeability measurements [14] which yielded

$$N_o^{(s)} D_o = 2.4 \times 10^{-4} \exp(-107.2 \text{ kJ}/RT) \text{ cm}^2 \text{ s}^{-1} \quad [6.32]$$

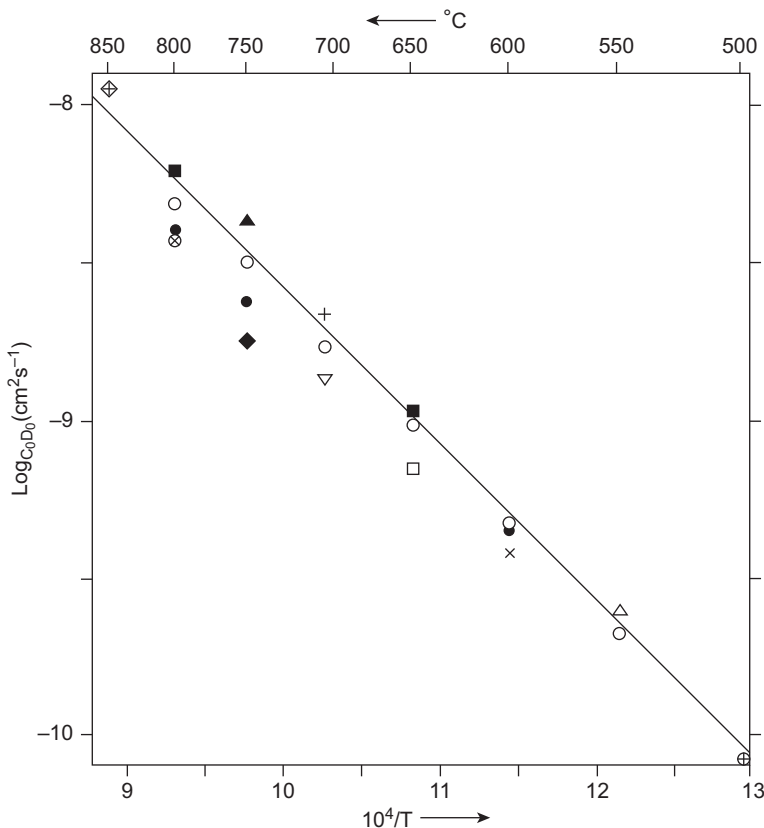


FIGURE 6.11 Permeability of oxygen in silver deduced from internal oxidation kinetics in 1 atm O_2 of: ■ Ag-1.3 Zn [6], □ Ag-1.0 Mg [6], ● Ag-1.75 Mg [15], ▲ Ag-1.8 Al [15], ◆ Ag-1.0 Cd [15], ◊ Ag-0.95 Cd [16], ▽ Ag-4.8 Cd [17], × Ag-1.7 Li [18], + Ag-0.3 Pb [19], ○ Ag-In alloys [20]. Continuous line represents Eq. [6.32]. Published from J.L. Meijering, in: H. Herman (Ed.), *Advances in Materials Research*, Wiley-Interscience, New York (1971), 1, with permission from Wiley.

Agreement is seen to be good. It may be concluded that, at least for the dilute alloys involved here, the assumption that oxide precipitates do not interfere with oxygen diffusion is reasonable. The internal oxidation of silver alloys is of more than academic interest: the process is used to provide hardness in silver based electrical contact materials.

Good quality data for oxygen permeability in nickel have been provided by Park and Altstetter [22], using solid-state electrochemical techniques to measure independently

$$D_0 = 4.9 \times 10^{-2} \exp(-164 \text{ kJ mol}^{-1}/RT) \text{ cm}^2 \text{ s}^{-1} \quad [6.33]$$

$$N_0^{(s)} = 8.3 \times 10^{-2} \exp(-55 \text{ kJ mol}^{-1}/RT) \quad [6.34]$$

for p_{O_2} set by the Ni/NiO equilibrium. Internal oxidation kinetics for various nickel base alloys have been used to deduce the oxygen permeability values shown in Fig. 6.12. Agreement with Eqs [6.33] and [6.34] is seen to be reasonable. It should be noted that permeabilities deduced from internal oxidation of Ni-Al alloys were in fact a function of $N_{Al}^{(o)}$, as will be discussed shortly. The values shown in Fig. 6.12 were obtained [21] by extrapolating to $N_{Al}^{(o)} = 0$.

Another prediction available from Eq. [6.10] is that for a given matrix A, fixed T and p_{O_2} , the rate constant for internal oxidation is inversely proportional to $N_B^{(o)}$. Internal oxidation rates for a series of Fe-Cr alloys [23] are seen

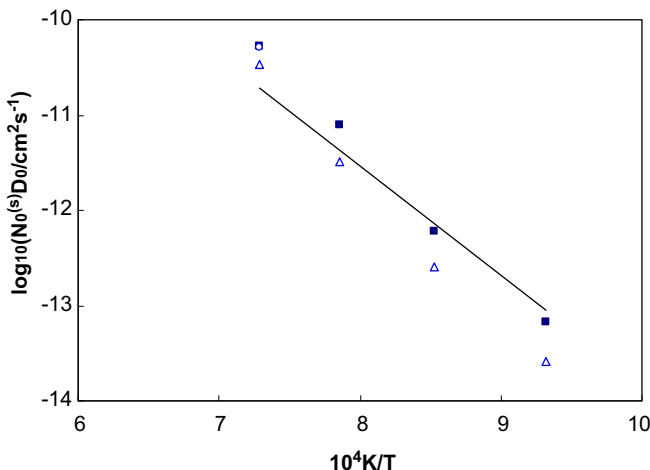


FIGURE 6.12 Permeability of oxygen in nickel deduced from internal oxidation kinetics under Rhines pack conclusions: ■ Ni-Cr [21], △ Ni-Al [21], ○ Ni-0.12Al [11]. Continuous line represents $N_0^{(s)} D_0$ according to Eqs. [6.33] and [6.44]. Published from J.L. Meijering, in: H. Herman (Ed.), *Advances in Materials Research*, Wiley-Interscience, New York (1971), 1, with permission from Wiley.

in Fig. 6.13 to vary with $1/N_{\text{Cr}}^{(0)}$ as predicted. Internal oxidation depths observed in Ni-Cr [21] and Cu-Si [24] alloys are seen in Fig. 6.14 to vary as predicted from Eqs [6.1] and [6.11], ie, $X_{(\text{i})}^2 \propto 1/N_{\text{B}}^{(0)}$.

As we have seen, the Wagner diffusion theory achieves considerable success in quantitatively accounting for internal oxidation rates. The theory also applies to internal attack by other oxidants, although reaction rates can be very different because of the different permeabilities. Some comparative data in Table 6.2 illustrate this point. The corresponding internal precipitation reaction rates are shown in Table 6.3. These data are plotted according to Eq. [6.10] in Fig. 6.15, using logarithmic scales to encompass the large ranges of values. The slope is close to unity, confirming that Eq. [6.10] provides a very useful predictive tool.

Despite the considerable successes of the Wagner diffusion model in describing internal precipitation reactions in the absence of any external scale, its applicability is limited by the assumptions on which it is based. The assumptions which may prove incorrect for some reacting systems are as follows:

- The precipitate is extremely stable, and both N_{o} and N_{B} are vanishingly small within the precipitation zone.
- As a consequence of (a), f_{BO} is constant throughout the precipitation zone and changes discontinuously to zero at the reaction front.

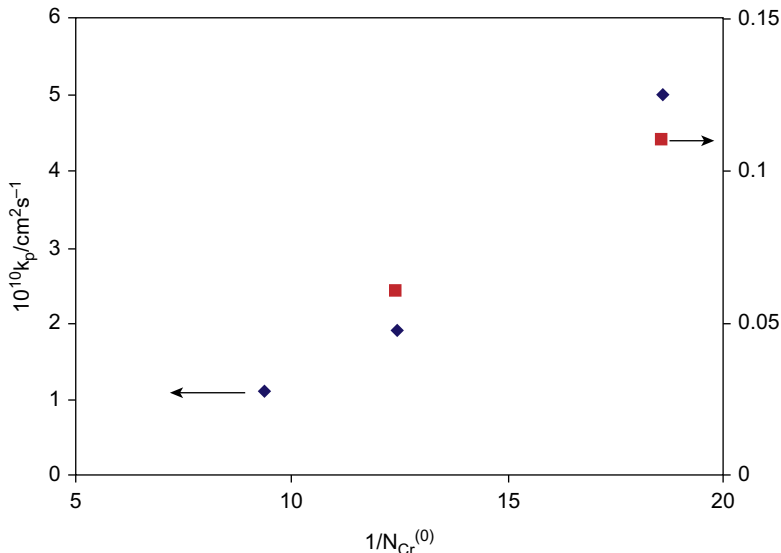


FIGURE 6.13 Internal oxidation rates for Fe-Cr alloys at $p_{\text{O}_2} = 8.7 \times 10^{-17} \text{ atm}$ (◆) and $2.6 \times 10^{-20} \text{ atm}$ (■). Published with permission from D.J. Young, O. Ahmed, Mater. Sci. Forum 369–372 (2001) 93, Trans Tech Publications.

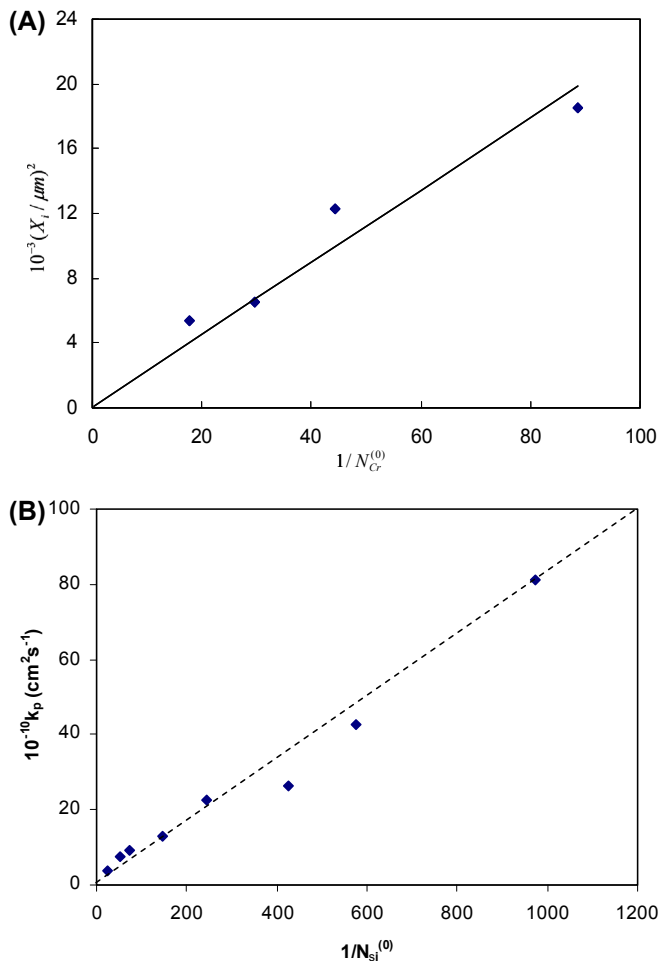


FIGURE 6.14 (A) Internal oxidation depth as a function of alloy solute content in Ni-Cr alloys in a Rhines pack at 1100°C for 10 h. (*Published with permission from D.P. Whittle, Y. Shida, G.C. Wood, F.H. Stott, B.D. Bastow, Phil. Mag. A 46 (1982) 931, Taylor & Francis Ltd., <http://www.tandf.co.uk/journals>.*) (B) Cu-Si alloy internal oxidation rates in a Rhines pack at 750°C. (*Published with permission from F.N. Rhines, W.A. Johnson, W.A. Anderson, Trans. AIME 147 (1942) 205, The Minerals, Metals & Materials Society.*)

- c. Precipitate nucleation and growth have no effect on overall reaction kinetics.
- d. Mass transfer within the internal oxidation zone occurs solely via lattice (bulk) diffusion, is unaffected by the presence of precipitates and is not subject to cross-effects resulting from kinetic or thermodynamic interactions with other solutes.

TABLE 6.2 Comparative Permeabilities ($\text{cm}^2 \text{s}^{-1}$) for Different Oxidants at 1000°C: Oxygen in Rhines Packs, Carbon at $a_c = 1$ and Nitrogen at $p_{\text{N}_2} = 1 \text{ atm}$

| Solvent Metal | $N_o^{(s)} D_o^{\text{a}}$ | $N_N^{(s)} D_N$ | $N_C^{(s)} D_C$ |
|---------------|----------------------------|-------------------------------|------------------------------|
| Ni | 4.3×10^{-12} | 1.5×10^{-11} [25,26] | 3.1×10^{-9} [27,28] |
| γ -Fe | 2.4×10^{-12} | 1.6×10^{-11} [25,26] | 1.4×10^{-8} [27,28] |

^aOxygen permeability data from Chapter 2.

TABLE 6.3 Comparative Internal Oxidation, Nitridation and Carburisation Rate Constants, $k_p^{(i)}$ ($\text{cm}^2 \text{s}^{-1}$) at 1000°C

| | Oxidation ^a | Nitridation ^b | Carburisation ^c |
|------------------------|--|---------------------------|----------------------------|
| α -Fe-5Cr | 5×10^{-10} (8.7×10^{-17} atm) [23] | | 2.4×10^{-7} [23] |
| γ -Ni-5Cr | 1×10^{-10} (4.7×10^{-11} atm) [29] | | |
| γ -Fe-20Ni-25Cr | | 6.6×10^{-9} [30] | 1.1×10^{-7} [30] |

^aat indicated p_{O_2} values.

^bat $p_{N_2} = 0.9 \text{ atm}$.

^cat $a_c = 1$.

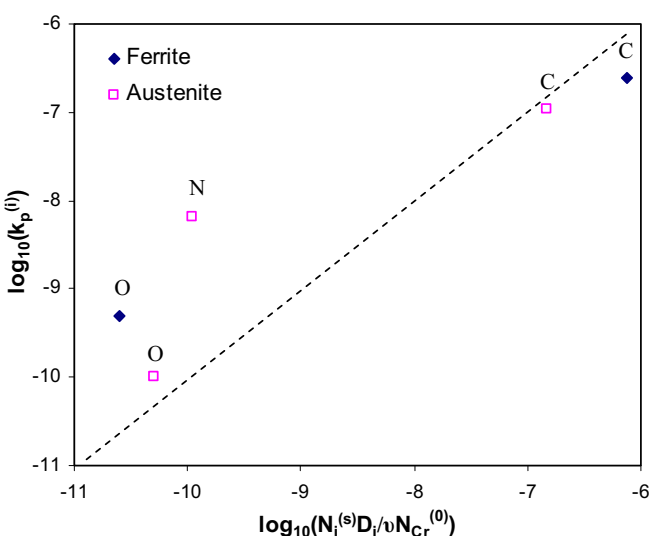


FIGURE 6.15 Internal precipitation reaction rates for different oxidants in ferritic and austenitic alloys under reaction conditions specified in Table 6.3.

We consider first the effect of precipitates, and microstructure in general, on oxidant diffusion, whilst retaining the assumptions of a highly stable precipitate and a matrix which is strongly depleted in reactive solute B.

6.5 SURFACE DIFFUSION EFFECTS IN THE PRECIPITATION ZONE

As seen in Figs 6.1 and 6.5, internal oxidation can be favoured at alloy grain boundaries. The situations in the two cases depicted are quite different. Although the precipitates formed on grain boundaries in Fe-Cr are larger, the penetration depth is the same as within the grains themselves, and the overall reaction kinetics are not affected. The austenitic alloy IN 617, however, has undergone rapid, preferential intergranular attack, forming a continuous internal oxide network along the grain boundaries. Preferential intergranular penetrations of internal oxide have been observed for Ni-Al alloys [31–34] and Ni-Cr alloys [35,36], to an extent which becomes more marked at lower temperatures and higher $N_B^{(o)}$ values. Intergranular morphologies of internal oxidation were reported earlier for Fe-Al [37], tin-based alloys [5] and copper-based alloys [4]. A related phenomenon is the in situ oxidation of prior interdendritic carbides in cast materials [38], shown in Fig. 6.16.

Intergranular oxidation can be much faster than the rate at which the intragranular precipitation front advances. The parabolic rate constant for intergranular oxidation in Ni-5Cr at 1000°C was found [21] to be about 10^3 times the value of $k_p^{(i)}$. Similarly, the rate of in situ carbide oxidation in cast heat-resisting steels (Fig. 6.16) has been observed [38,39] to be much faster than intragranular precipitation. Clearly, these rapid rates cannot be sustained by volume (lattice) diffusion of oxygen, and a faster transport process must be involved. A model based on diffusion along the oxide-metal grain boundary is shown schematically in Fig. 6.17 for the case of in situ carbide oxidation.

A very similar situation arises when intragranular precipitates form with elongated plate or rod shapes, aligned in the growth direction (Fig. 6.7). The example of elongated Al_2O_3 precipitate growth in dilute Ni-Al alloys has been studied intensively [21,29,40–46], leading to an understanding of the diffusion processes involved in the growth of these cellular morphologies. The kinetics of internal oxidation are parabolic, reflecting diffusion control, but the rate constant is independent of $N_{\text{Al}}^{(o)}$. The behaviour of these alloys is compared with that of Ni-Cr in Fig. 6.18. As is obvious, the data for Ni-Cr alloys conform with Eq. [6.11], but those for Ni-Al do not. If, nonetheless, effective oxygen permeability values are deduced from Eq. [6.11], they are found [29] apparently to increase with aluminium levels

$$N_o^{(s)} D_o(\text{eff}) = a + b N_{\text{Al}}^{(o)} \quad [6.35]$$

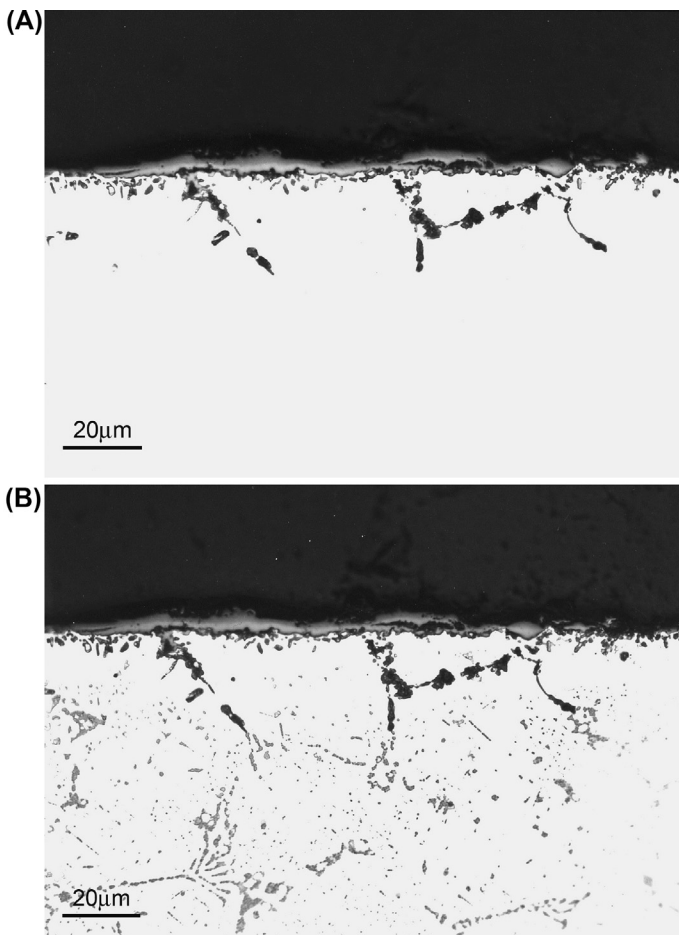


FIGURE 6.16 Rapid penetration of internal oxide along prior carbide network in cast Fe-35Ni-27Cr alloy at $T = 1000^\circ\text{C}$. (A) unetched and (B) stain etched to reveal carbides [39]. With kind permission from Springer Science and Business Media.

where a and b are constants. This is interpreted to mean that oxygen diffuses both through the metal matrix and along precipitate-matrix interfaces, the concentration of the latter being proportional to the original alloy aluminium content. On this basis, the effective flux of oxygen through a precipitation zone containing lath-shaped oxides oriented as shown in Fig. 6.19 can be written

$$J_{\text{eff}} = J_o A_o + J_i A_i + J_{\text{ox}} A_{\text{ox}} \quad [6.36]$$

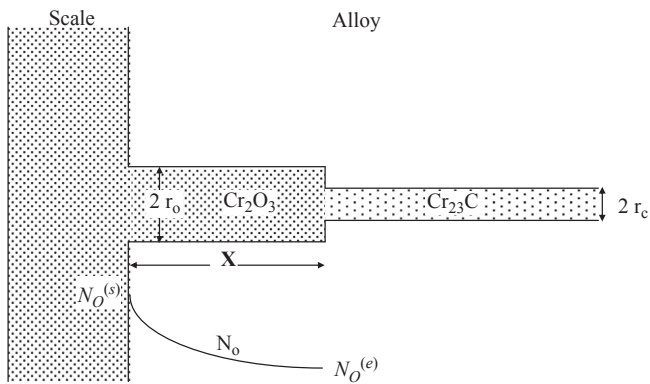


FIGURE 6.17 Schematic model for enhanced internal boundary oxidation of prior carbide in situ. With kind permission from P. Becker, M. Panasko, D.J. Young, *Oxid. Met.* 64 (2005) 281, Springer Science and Business Media.

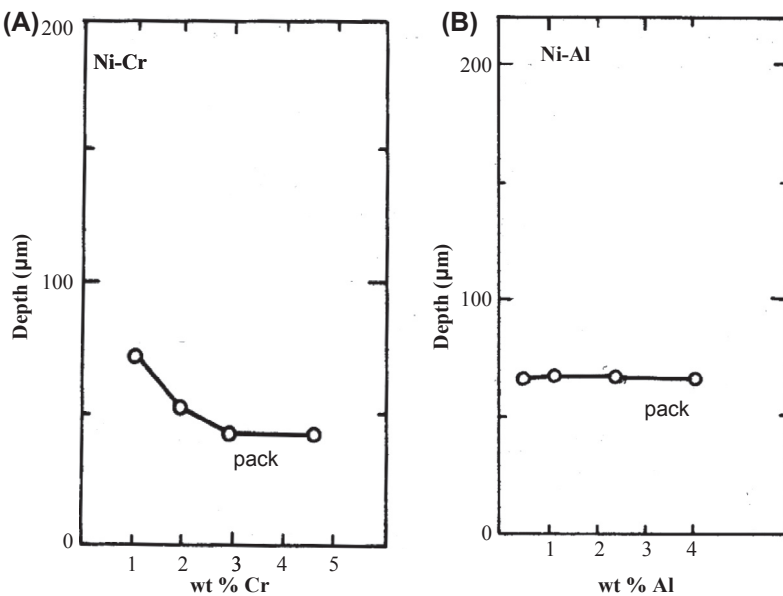


FIGURE 6.18 Internal oxidation of (A) Ni-Cr and (B) Ni-Al alloys in Rhines packs for 20 h at 1000°C. Plot based on data from D.P. Whittle, Y. Shida, G.C. Wood, F.H. Stott, B.D. Bastow, *Phil. Mag. A* 46 (1982) 931. Published with permission from Taylor & Francis Ltd., <http://www.tandf.co.uk/journals>.

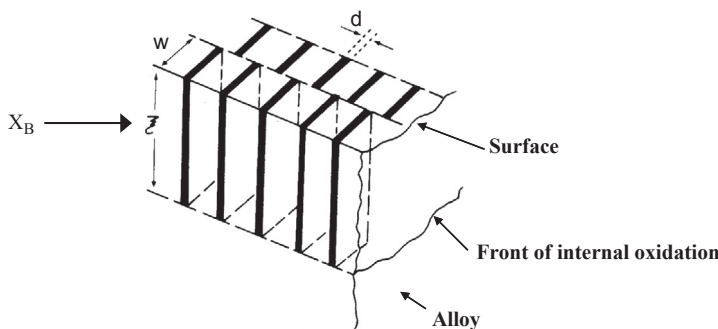


FIGURE 6.19 Schematic view of oriented Al_2O_3 laths in internal oxidation zone. Published with permission from D.P. Whittle, Y. Shida, G.C. Wood, F.H. Stott, B.D. Bastow, *Phil. Mag. A* 46 (1982) 931, Taylor & Francis Ltd., <http://www.tandf.co.uk/journals>.

where A_o , A_i and A_{OX} are the cross-sectional area fractions of alloy, alloy-oxide interface and oxide, normal to the diffusion direction. Because diffusion in Al_2O_3 is so slow, the third term is set at zero. The effective oxygen diffusion coefficient is then defined as

$$D_{\text{eff}} = D_{o,o}A_o + D_{o,i}A_i \quad [6.37]$$

where $D_{o,o}$ is the usual diffusion coefficient of oxygen in nickel and $D_{o,i}$ is the interfacial coefficient. The area fractions and diffusion coefficients are assumed to be independent of position within the internal oxidation zone. The mole fraction of oxide is related to the precipitate dimensions and their number density, F_N . Using the dimensions specified in Fig. 6.19 and assuming that the precipitates are continuous across the full width of the internal oxidation zone, we write

$$N_{\text{BO}} = F_N w d \frac{V_{\text{All}}}{V_{\text{OX}}} \quad [6.38]$$

and

$$A_i = 2(w + d)F_N \delta_i \approx 2wF_N \delta_i \quad [6.39]$$

where δ_i is the width of the interface diffusion zone and the approximation is based on $w \gg d$.

The cross-section of matrix metal remaining after oxide precipitation is

$$A_o = 1 - A_i - A_{\text{OX}} = 1 - 2wF_N \delta_i - F_N w d \quad [6.40]$$

which, upon substitution along with Eqs [6.38] and [6.39] into Eq. [6.37] yields

$$\frac{D_{o,\text{eff}}}{D_{o,o}} = 1 + \left[\frac{D_{o,i}\delta_i}{D_{o,o}} \cdot \frac{2}{d} - 1 \right] \frac{V_{\text{OX}}}{V_{\text{All}}} N_{\text{BO}} \quad [6.41]$$

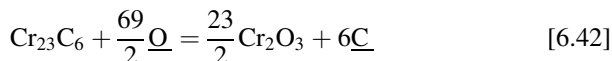
TABLE 6.4 Interfacial and Matrix Oxygen Diffusion in Internally Oxidised Ni-Al [21] ^a

| T (°C) | $D_{o,i}\delta_i/D_{o,o}d$ | $D_{o,i}/D_{o,o}$ |
|----------|----------------------------|------------------------------|
| 1100 | 39 | $3.9\text{--}39 \times 10^2$ |
| 1000 | 85 | $8.5\text{--}85 \times 10^2$ |
| 900 | 85 | $8.5\text{--}85 \times 10^2$ |
| 800 | 173 | $1.7\text{--}17 \times 10^3$ |

^a $D_{o,i}/D_{o,o}$ calculated for $d = 10\text{--}100$ nm and δ_i assumed to be 1 nm.

A similar result was obtained for rod-shaped precipitates [21,29] and indeed will be found for any prismatic precipitate morphology. If no aluminium enrichment occurs, the amount of oxide corresponds to the original alloy concentration, $N_{BO} = N_{Al}^{(o)}$, then the form of Eq. [6.41] is seen to correspond with the experimental result Eq. [6.35]. Comparison of experimentally determined values for b with the corresponding term in Eq. [6.35] yielded the results shown in Table 6.4.

The ratios between interfacial and lattice diffusion coefficients of oxygen seem reasonable and increase with decreasing temperature as would be expected. If the interfaces concerned are incoherent, as was assumed [21], then the chemical identity of the oxide will be of secondary importance, and a similar enhancement in oxygen diffusion can be anticipated for any oxide-austenite interface. The example of in situ oxidation of interdendritic chromium carbide (Fig. 6.16) is now analysed on this basis. As is clear in the micrograph, oxygen penetration at the interdendritic locations was much faster than within the austenite grains, where only a shallow internal oxidation zone had formed. Oxidation of a rod-shaped carbide is shown schematically in Fig. 6.17. The chemical reaction



is accompanied by a volume expansion. If accumulation of chromium from the surrounding metal matrix can be ignored, the rod radii are related by

$$r_o = kr_c \quad [6.43]$$

where the subscripts denote oxide or carbide, and k is the ratio

$$k = 11.5V_{\text{OX}}/V_c \quad [6.44]$$

with V_i the molar volume of the indicated substance.

In the figure, N_o denotes the local concentration of oxygen, and the zone of rapid inward interfacial diffusion is defined as an annular region, of width δ , around the oxide rod. Boundary values of the oxygen concentration are set at the alloy-scale interface, $N_o^{(s)}$, and by local carbide-oxide equilibrium, $N_o^{(e)}$.

The molar flux of oxygen, J_o , per unit cross-sectional area of carbide rod is given by the linear approximation to Fick's Law as

$$J_o = \frac{\delta(2r_o + \delta)}{r_c^2} \frac{D_{o,i}}{V_A} \frac{(N_o^{(s)} - N_o^{(e)})}{X_B} \quad [6.45]$$

where r is the rod radius, $D_{o,i}$ the interfacial diffusion coefficient, V_A the alloy matrix molar volume and X_B the boundary oxidation depth. If this oxygen is entirely consumed in reaction with the carbide rod, then the resulting oxide rod lengthens at a rate given by

$$\frac{dX_B}{dt} = \frac{J_o}{69/2} \cdot V_c \quad [6.46]$$

Combination of Eqs [6.43]–[6.46] leads to

$$\frac{dX_B}{dt} = \frac{2}{3} \frac{\delta D_{o,i}}{r_c} \frac{V_{OX}}{V_A} \frac{N_o^{(s)} - N_o^{(e)}}{X_B} \quad [6.47]$$

for the case $\delta \ll r_c$. Integration of Eq. [6.47] leads to

$$X_B^2 = 2k_B^{(i)} t \quad [6.48]$$

where the parabolic rate constant for internal oxidation

$$k_B^{(i)} = \frac{2}{3} \frac{\delta D_{o,i}}{r_c} \frac{V_{OX}}{V_A} \left(N_o^{(s)} - N_o^{(e)} \right) \quad [6.49]$$

is independent of primary carbide volume fraction, but inversely proportional to carbide diameter. A similar conclusion is reached if other prismatic carbide shapes, such as uniform sheets, are chosen. Inward oxygen diffusion along phase boundaries according to Eq. [6.49] explains the observation [38] that several heat-resisting alloys all had approximately the same internal oxide penetration rates, despite their considerable variations in composition.

Comparing the interdendritic oxidation rate constant of [6.49] with the normal bulk material value of [6.10], we obtain

$$\frac{k_B^{(i)}}{k_p^{(i)}} = \frac{N_{Cr}^{(o)} V_{OX}}{r_c V_A} \frac{\delta_i D_{o,i}}{D_{o,o}} \quad [6.50]$$

if $N_o^{(e)} \ll N_o^{(s)}$. The value of $k_B^{(i)}$ measured for an austenitic Fe-35Ni-27Cr cast steel at 1000°C was $3 \times 10^{-11} \text{ cm}^2 \text{ s}^{-1}$ compared with the value

$k_p^{(i)} = 6 \times 10^{-18} \text{ cm}^2 \text{ s}^{-1}$ expected for lattice diffusion under the same conditions. Substitution of these values in Eq. [6.50] together with $r_c = 2 \mu\text{m}$ and $N_{\text{Cr}}^{(o)} = 0.29$ leads to the estimate $\delta_i D_{\text{o},i}/D_{\text{o},o} = 800$. This is similar to estimates of boundary diffusion along Al_2O_3 -austenite interfaces (Table 6.4).

As seen in Table 6.4, enhancement of oxygen diffusion at boundaries is of decreased importance at higher temperatures. Hindam and Whittle [42] showed that at 1200°C, lath or rod-shaped precipitates (depending on $N_{\text{Al}}^{(o)}$) grew into dilute Ni-Al alloys according to parabolic kinetics, but at rates which were controlled by oxygen diffusion through the matrix. Thus it can be concluded that boundary diffusion of an oxidant is not a necessary condition for the development of a cellular precipitation morphology. Because the elongated precipitate-matrix interfaces have the effect of accelerating internal attack at lower temperatures, the question of how to predict their formation is an important one to which we return in Section 6.8.

Finally, it should be noted that the precipitates formed during internal oxidation of dilute chromium and aluminium alloys are in fact more complex than has been implied. In both cases a spinel phase, MCr_2O_4 or MAl_2O_4 , is formed near the surface if the oxygen activity is high enough. The binary oxide, M_2O_3 , forms in a second, deeper precipitation zone. The general question of multiple precipitation zones is discussed in Section 6.9.

When the internally formed precipitates are small and disperse, their surfaces cannot provide any significant contribution to diffusion. However, their presence reduces the metal matrix cross-section available for diffusion, as stated in Eq. [6.40]. For this reason, it is common to rewrite Eq. [6.10] as

$$k_p^{(i)} = \frac{\varepsilon D_o N_o^{(s)}}{v N_B^{(o)}} \quad [6.51]$$

where ε is an empirical constant designed to take into account the diffusional blocking effect of the precipitates. The quantity ε would be expected to be related to f_{BO} , but no information is available on this point, possibly because precipitate fractions are often small, and $\varepsilon \approx 1$.

6.6 INTERNAL PRECIPITATES OF LOW STABILITY

The Wagner diffusion model assumes K_{sp} vanishingly small and both N_o and N_B extremely dilute within the precipitation zone, which is therefore essentially oxide embedded in pure solvent metal A. However, this is not a realistic description for many cases. Consider precipitation of chromium compounds within an alloy



$$K_{\text{sp}} = N_{\text{Cr}}^a N_{\text{X}}^{va} \quad [6.53]$$

where X is a generic oxidant and K_{sp} is the equilibrium solubility product. If K_{sp} is not extremely small, then the necessarily low values of N_X mean that N_{Cr} will not always be small, and the assumption of complete precipitation fails. Even for rather stable precipitates, such as Cr_2O_3 , this condition can be difficult to meet at low oxidant activities.

Values for K_{sp} are calculated for Eq. [6.52] using the free energies of compound formation and alloy dissolution



using tabulated values [47] for oxide and carbide formation, together with Rosenqvist's data [48] for $\Delta G_f^\circ(\text{Cr}_2\text{N})$. Measured carbon [28] and oxygen (Table 2.2) solubility data are available, but the situation for nitrogen is less clear. Although the expression

$$\Delta \overline{G}_{\text{N}_2}(\gamma - \text{Fe}) = -5690 + 118.6T + 2RT \ln N_{\text{N}} \text{ J/mol} \quad [6.57]$$

is available [47], it is recognised that no accurate data are available for Ni-N solutions. Following Savva et al. [49] in conjecturing a temperature insensitive solubility of 1 ppma, we find

$$\Delta \overline{G}_{\text{N}_2}(\text{Ni}) = 292,460 + 2RT \ln N_{\text{N}} \text{ J/mol} \quad [6.58]$$

These estimates, together with partial molar free energies of solution of chromium in iron [47], lead to the precipitate stability data shown in Tables 6.5 and 6.6.

The quantity $N_{\text{Cr,min}}$ in the tables is the minimum concentration (mole fraction) of chromium required in the matrix metal to stabilise the designated precipitate at the alloy surface where N_X has its maximum value of $N_X^{(s)}$. Clearly the assumption of complete precipitation is in considerable error for the chromium carbides and nitride. Even the rather stable oxide precipitates, leaving a significant concentration of chromium in the alloy. The temperature effect is significant, both through the decreased oxide stability at higher temperature and the retrograde oxygen solubility. The calculated results of Table 6.6 correspond to greatly decreased extents of chromium precipitation at higher temperatures. This effect is apparent in the internal oxidation of Fe-Cr alloys (Fig. 6.1), where the volume fraction of oxide decreases substantially at higher temperatures.

It is recognised that the calculated $N_{\text{Cr,min}}$ values apply at the alloy surface. As depth within the precipitation zone increases, N_o must decrease, and therefore the concentration of chromium in the matrix, N_{Cr} , must increase in order to stabilise the precipitate, according to [6.53]. The amount of oxide

TABLE 6.5 Chromium Compound Precipitate Solubilities at 1000°C in γ -Fe

| | Cr_2O_3 | | Carbides ($a_c = 1$) | | Nitride |
|-----------------------------|--|--|-------------------------|----------------------------|---|
| | $p_{\text{O}_2} = 8.7 \times 10^{-17}$ atm | $p_{\text{O}_2} = 2.6 \times 10^{-20}$ atm | Cr_7C_3 | Cr_{23}C_6 | Cr_2N at $p_{\text{N}_2} = 1$ atm |
| $N_{\text{X}}^{(\text{s})}$ | 3.5×10^{-6} | 6×10^{-8} | 0.066 | 0.066 | 1×10^{-3} |
| K_{sp} | 1.4×10^{-25} | 1.4×10^{-25} | 3.8×10^{-15} | 3.6×10^{-27} | 3×10^{-5} |
| $N_{\text{Cr,min}}$ | 6×10^{-5} | 0.02 | 0.03 | 0.14 | 0.17 |

TABLE 6.6 Cr_2O_3 Solubilities in γ -Fe at Low p_{O_2} Values (atm)

| T (°C) | 900 | | 1000 | | 1100 | |
|-----------------------------|-----------------------|-----------------------|-----------------------|-----------------------|-----------------------|-----------------------|
| p_{O_2} /atm | 8.7×10^{-17} | 2.6×10^{-20} | 8.7×10^{-17} | 2.6×10^{-20} | 8.7×10^{-17} | 2.6×10^{-20} |
| $N_{\text{o}}^{(\text{s})}$ | 6.8×10^{-6} | 1.2×10^{-7} | 3.5×10^{-6} | 6×10^{-8} | 1.6×10^{-6} | 2.8×10^{-8} |
| K_{sp} | 1.1×10^{-27} | | 1.4×10^{-25} | | 8.6×10^{-24} | |
| $N_{\text{Cr,min}}$ | 2×10^{-6} | 8×10^{-4} | 6×10^{-5} | 0.02 | 1×10^{-3} | 0.62 |

precipitated, f_{BO} , must therefore be a function of position, decreasing from a maximum at the alloy surface to a minimum at the reaction front. In view of this, it is necessary to investigate the effect of incomplete precipitation on the practically important quantity: the rate at which the internal oxidation front advances. Qualitatively, the consequence is clear. A lower value of f_{BO} reflects, in effect, a reduced availability of chromium, ie, an effectively lower value of $N_{\text{B}}^{(o)}$ in Eq. [6.11] and hence larger values of $k_p^{(i)}$.

The precipitate volume fraction varies with position, reflecting the changing values of N_{o} and N_{Cr} . Schematic concentration profiles are shown in Fig. 6.20, with a diffusion path for Cr_2N precipitation. The equilibrium fraction of precipitate can be related to composition via the lever rule:

$$f_{\text{BO}} = \left(N_{\text{B}}^{(o)} - N_{\text{B}} \right) / \left(N_{\text{B}}^{\text{p}} - N_{\text{B}} \right) \quad [6.59]$$

where N_{B}^{p} and N_{B} refer to local values in the precipitate and matrix respectively, and negligible diffusion of B has been assumed. Defining a precipitate fraction r , normalised to its value at the alloy surface

$$r = \left(N_{\text{B}}^{(o)} - N_{\text{B}} \right) / \left(N_{\text{B}}^{(o)} - N_{\text{B}}^{(s)} \right) \quad [6.60]$$

and recognising that the local equilibrium is described by combining Eqs [6.53] and [6.60], we obtain

$$\frac{N_{\text{B}}}{N_{\text{B}}^{(o)}} = 1 - \alpha r \quad [6.61]$$

with the solubility parameter

$$\alpha = 1 - K_{\text{sp}}^{1/a} / N_{\text{B}}^{(o)} \left(N_{\text{X}}^{(s)} \right)^v \quad [6.62]$$

For Wagner's equation (Eq. [6.10]) to apply, precipitation must be uniform and complete, ie, $r \rightarrow 1$ and $N_{\text{B}} \rightarrow 0$. From Eq. [6.61], it is seen that this requires $\alpha \rightarrow 1$, a condition met when $K_{\text{sp}} \ll \left(N_{\text{B}}^{(o)} \right)^a \left(N_{\text{X}}^{(s)} \right)^{av}$, a condition which will not be met for chromium carbide or nitride.

The diffusional kinetics of this situation were analysed by Kirkaldy [50] and independently by Ohriner and Morral [51], and they have been applied to the specific case of Cr_2N in Fe-Cr [52]. Assuming still that metal diffusion is unimportant and that $K_{\text{sp}} \gg N_{\text{N}}^3$, one obtains

$$\frac{\partial r}{\partial t} = \frac{4K_{\text{sp}}D_{\text{N}}}{\left(N_{\text{Cr}}^{(o)} \right)^3} \frac{\partial}{\partial x} \left\{ \frac{1}{(1 - \alpha r)^2} \frac{\partial r}{\partial t} \right\} \quad [6.63]$$

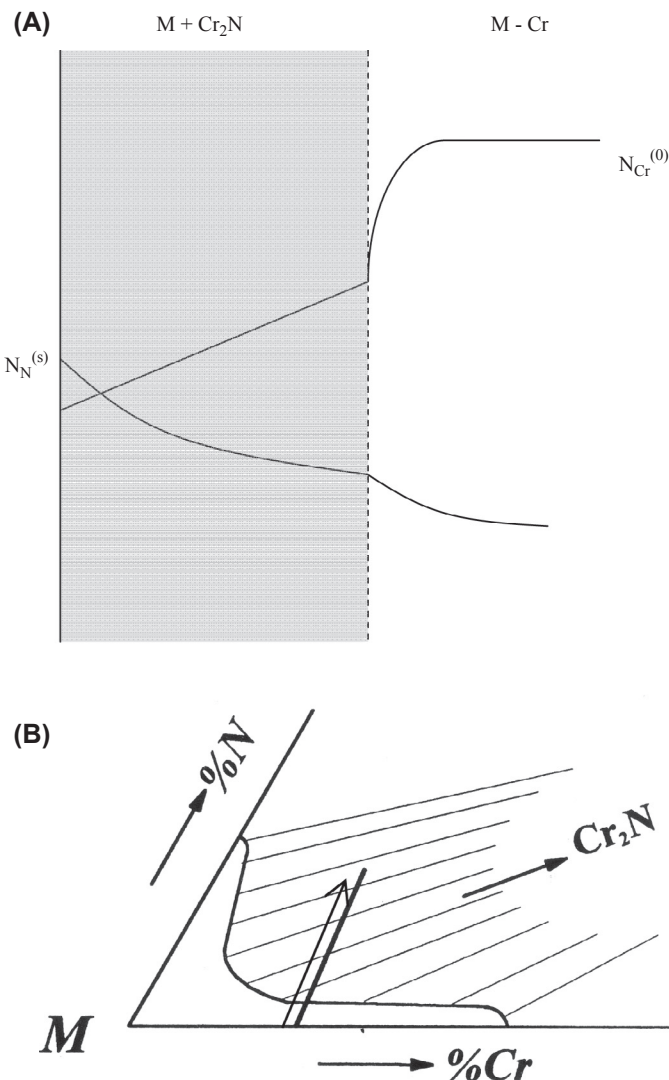


FIGURE 6.20 Formation of low stability Cr_2N precipitates: (A) concentration profiles and (B) diffusion path for $D_{\text{N}} \gg D_{\text{Cr}} \approx 0$.

This equation can be converted via the Boltzmann transformation ($\lambda = x/\sqrt{t}$) to an ordinary differential equation which upon integration yields

$$\frac{(1-\alpha)^2}{(1-\alpha r)^2} = \frac{N_{\text{Cr}}^{(0)}}{8D_{\text{N}} t N_{\text{N}}^{(s)}} \frac{dx}{dr} \int_0^{r'} x dr \quad [6.64]$$

where r' is the value chosen in the interval $[0,1]$ for evaluation.

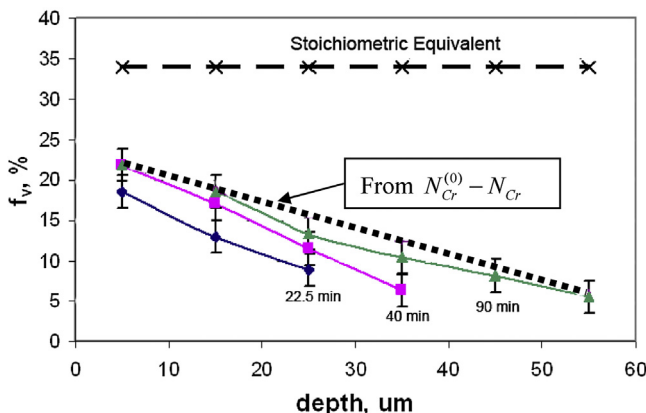


FIGURE 6.21 Nitride volume fractions in internally nitrided Fe-25Cr-20Ni at 1000°C, compared with stoichiometric equivalent of $N_{\text{Cr}}^{(0)}$, and calculated from mass balance, assuming no Cr diffusion.

The variation in Cr_2N volume fraction f_v with depth in an internally nitrided alloy, is shown in Fig. 6.21. The value of f_v decreases approximately linearly with depth and is everywhere much lower than the stoichiometric equivalent of $N_{\text{Cr}}^{(0)}$. Also shown in the figure is the value of f_v calculated from TEM-EDAX measurements of N_{Cr} as a function of depth in the matrix of the internal nitridation zone. This calculation is based on the assumption that chromium diffusion is negligible, and the difference $(N_{\text{Cr}}^{(0)} - N_{\text{Cr}})$ is therefore equivalent to the amount of nitride precipitated. Agreement is seen to be excellent, confirming that chromium diffusion can be neglected.

Application of Eq. [6.64] requires knowledge of several parameters. Unfortunately, the assumption of ideal solution behaviour, ie, $N_{\text{N}}^{(\text{s})} \neq f(N_{\text{Cr}})$ is incorrect, as will be discussed in Section 6.10. For the moment, however, it is sufficient to use the effective permeability $N_{\text{N}}^{(\text{s})} D_{\text{N}} = 8.8 \times 10^{-10} \text{ cm}^2 \text{ s}^{-1}$ at 1000°C and $p_{\text{N}_2} = 0.9 \text{ atm}$, as deduced from internal nitridation kinetics [53]. The solution of Eq. [6.64] using this permeability value and the measured $r = r(x)$ in Fig. 6.21 yields $\alpha = 0.82$. The corresponding value of $K_{\text{sp}}(\text{Cr}_2\text{N})$ is then calculated from Eq. [6.62] using the nitrogen solubility $N_{\text{N}}^{(\text{s})}$. If the effect of residual chromium on nitrogen solubility is ignored, then a value of $K_{\text{sp}} = 6 \times 10^{-7}$ results. The values calculated thermodynamically from the method of Eqs [6.54]–[6.56] are 3×10^{-5} in $\gamma = \text{Fe}$ and 2×10^{-8} in nickel. The agreement between the value deduced from the precipitate distribution in Eq. [6.64] and the expected range for thermodynamic equilibrium is good. The semiquantitative success of the diffusion model implies that local equilibrium in the metal matrix (as expressed by Eq. [6.53]) is maintained by steady-state diffusion of dissolved nitrogen, and the local extent of precipitation is

therefore controlled by the precipitate-matrix equilibrium (Eq. [6.60] and Fig. 6.20). In short, the precipitate distribution is controlled by the diffusion path, ie, the diffusion coefficients and the phase diagram, and not by nucleation phenomena.

The extent to which internal nitrogen penetration exceeds the predictions of Eq. [6.11] depends on the deviation of r from the ideal value of 1, ie, on α . Ohriner and Morral [51] have calculated that for $\alpha = 0.8$ the quantity $X/t^{1/2}$ exceeds the model prediction by a factor of ~ 1.7 . This corresponds to an increase in k_p by a factor of about three. Experimentally measured [53] values of k_p are in fact up to five times faster than predicted from Eq. [6.11]. The additional acceleration is due to enhanced $N_N^{(s)}$ values enhanced by a thermodynamic interaction with solute chromium.

As we have seen, the Kirkaldy/Morral theory succeeds in describing the distribution of low stability precipitates. In order to gain an understanding of why precipitate sizes and number densities vary with position within the internal oxidation zone, it is necessary to examine the process of precipitate nucleation and growth.

6.7 PRECIPITATE NUCLEATION AND GROWTH

It has been assumed so far that the internal oxidation front corresponds to the position where the equilibrium (Eq. [6.2]) is just satisfied. However, new precipitates cannot form if Eq. [6.3] is precisely obeyed. In order to nucleate a new precipitate, an excess of oxidant is required

$$N_o > (K_{sp}/N_B)^{1/v} \quad [6.65]$$

to drive the nucleation event. The need for this supersaturation was recognised by Wagner [54], but it was not incorporated into his description.

The need for supersaturation can be understood from a consideration of the energetics of oxide nucleus formation. For simplicity, we consider first the formation of a spherical nucleus within a homogeneous, isotropic alloy matrix and assume for the moment that the molar volume of B is the same in both oxide and alloy. The overall free energy is

$$\Delta G = V\Delta G_V + A\gamma \quad [6.66]$$

where V is the volume of the precipitate, ΔG_V the free energy per unit volume accompanying the chemical reaction (Eq. [6.2]), A the surface area and γ the precipitate-matrix interfacial tension. For a spherical precipitate of radius r

$$\Delta G = \frac{4}{3}\pi r^3 \Delta G_V + 4\pi r^2 \gamma \quad [6.67]$$

which is represented schematically in Fig. 6.22. At small values of r , the second term is more important than the first, but at larger values the reverse is true. The shape of the curve in Fig. 6.22 reflects a negative value for ΔG_V and a

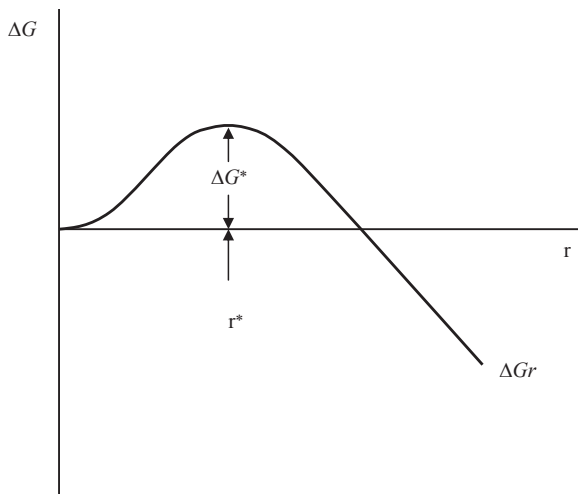


FIGURE 6.22 Free energy of spherical nucleus formation according to Eq. [6.67].

positive one for γ . As is seen for $r < r^*$, a nucleus will spontaneously decay, whereas for $r > r^*$, free energy is reduced by precipitate growth. For this reason, r^* is known as the critical nucleus size, and sufficient supersaturation must be present to provide ΔG_V large enough to overcome the surface energy barrier, ΔG^* , to nucleus formation.

The assumptions underlying Eq. [6.67] are unrealistic. Recognising that precipitates may not be spherical, that their volume will generally be larger than that of the metal they replace and that nucleation sites are usually local defects, we write instead

$$\Delta G = V(\Delta G_V + \Delta G_S) + \sum_i A_i \gamma_i - \Delta G_d \quad [6.68]$$

where ΔG_S is the strain energy resulting from the volume change, A_i and γ_i are the areas and surface tensions of the precipitate-matrix interfaces and ΔG_d is the energy associated with defect site annihilation. At equilibrium, ΔG_V just balances the strain and surface energy barriers to nucleation.

In the case of spherical precipitates, Eq. [6.68] can be rewritten as

$$\Delta G = \frac{4}{3} \pi r^3 (\Delta G_V + \Delta G_S) + 4\pi r^2 \gamma - \Delta G_d \quad [6.69]$$

The critical values r^* and ΔG^* are found by differentiating Eq. [6.69] to locate the maximum in the curve

$$r^* = \frac{2\gamma}{(\Delta G_V - \Delta G_S)} \quad [6.70]$$

$$\Delta G^* = \frac{16\pi\gamma^3}{3(\Delta G_V - \Delta G_S)} - \Delta G_d \quad [6.71]$$

where, for clarity, the fact that ΔG_V is of opposite sign to both ΔG_S and γ has been explicitly recognised. Thus the more stable the precipitate, the lower the barrier to nucleation.

The nature of the defect at which nucleation occurs is important, as the magnitude of ΔG_d can vary considerably. In order of increasing ΔG_d , ie, decreasing ΔG^* , the sequence would be approximately: homogeneous sites, vacancies, dislocations, stacking faults, grain and interphase boundaries and free surfaces. This is evident in the frequently observed preferential precipitation of internal oxides at alloy grain boundaries, eg, Figs 6.1 and 6.5.

The effects of the supersaturation requirement on precipitate size distributions and penetration kinetics were examined by Bohm and Kahlweit [16,55,56], and their treatment has since been extended by Gesmundo et al. [57]. The diffusion model is shown schematically in Fig. 6.23. A key difference between this description and that used by Wagner (Fig. 6.9) is that the precipitation front is not precisely defined but instead is spread over a small region wherein N_0 and N_B change with time as particles nucleate and grow. This can be appreciated from a consideration of mass transfer in the region of a newly formed precipitate (Fig. 6.24).

For the precipitate to develop, both \underline{O} and \underline{B} must be delivered to its surface. In the usual case of $N_B^{(0)}D_B \ll N_0^{(s)}D_o$, precipitate growth is limited by the availability of the metal, which becomes depleted ahead of the precipitate. A point is reached at which the oxide particle can grow no further, and the inwardly diffusing oxygen sweeps past it, deeper into the alloy. In order to form the next precipitate, sufficient supersaturation must be achieved

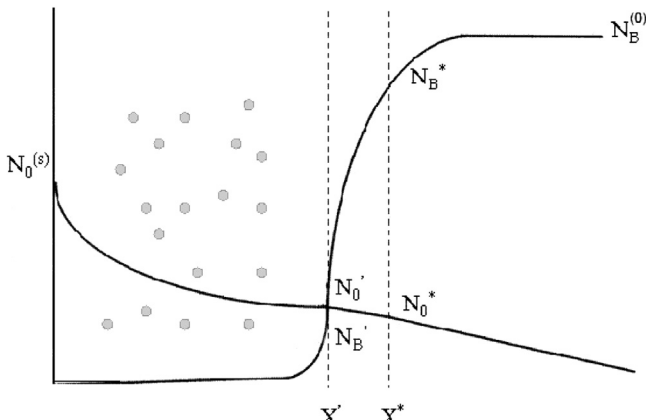


FIGURE 6.23 Schematic concentration profiles for internal precipitation of BO_x showing a supersaturated region ahead of the internal oxidation zone.

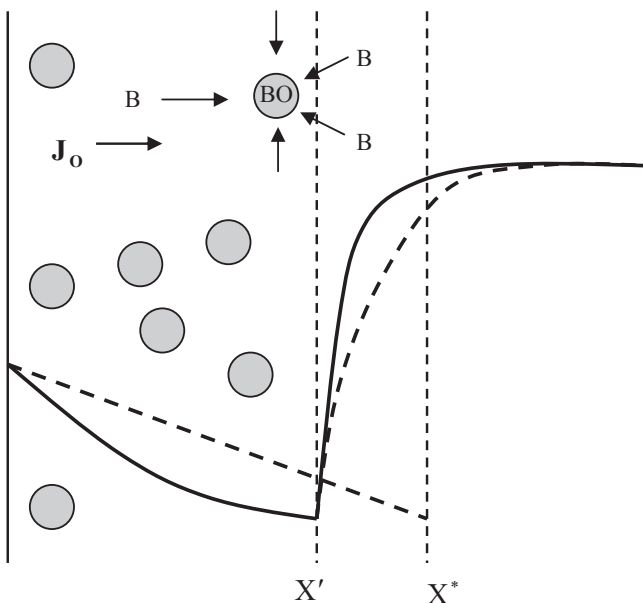


FIGURE 6.24 Mass transfer near a growing precipitate at the internal oxidation front: continuous concentration profiles at time of nucleation and dotted profiles after precipitate growth.

to overcome the nucleation barrier. At the position, X^* , where this is achieved, the reactant concentrations are denoted as N_o^* and N_B^* , and

$$N_B^* (N_o^*)^v = S^* > K_{sp} \quad [6.72]$$

In contrast, the last-formed precipitate relieved the local supersaturation when it nucleated, and at that location, X' ,

$$N'_B (N'_o)^v = K_{sp} \quad [6.73]$$

a relationship which is observed throughout the region $O \leq x \leq X'$.

For parabolic internal oxidation kinetics, the diffusion equation solutions [16] for the reactant concentrations are

$$N_o = N_o^{(s)} - \frac{N_o^{(s)} - N_o^*}{erf(\gamma)} erf\left(x/2\sqrt{D_o t}\right) \quad \text{for } x < X^* \quad [6.74]$$

and

$$N_B = N_B^{(o)} - \frac{N_B^{(o)} - N_B^*}{erfc\left(\gamma\phi^{\frac{1}{2}}\right)} erfc\left(x/2\sqrt{D_B t}\right) \quad \text{for } x > X^* \quad [6.75]$$

In general [57],

$$\frac{N_o^{(s)} - N_c^*}{N_B^{(o)} - N_B^*} = v \frac{G(\gamma)}{F(\gamma\phi^{\frac{1}{2}})} + \frac{N_B^* - N'_B}{N_B^{(o)} - N'_B} G(\gamma) \quad [6.76]$$

where

$$G(u) = \pi^{\frac{1}{2}} u \exp(-u^2) \operatorname{erf}(u) \quad [6.77]$$

and

$$F(u) = \pi^{\frac{1}{2}} u \exp(-u^2) \operatorname{erfc}(u) \quad [6.78]$$

with $u = \gamma\phi^{\frac{1}{2}}$ under the limiting conditions $\gamma^2 \ll 1$ and $N_o^* \ll N_o^{(s)}$, then $G(\gamma^2) \approx 2\gamma^2$, and then

$$k_p^{(i)} = \frac{D_o N_o^{(s)}}{v(N_B^{(o)} - N'_B)} \quad [6.79]$$

replaces Eq. [6.11], as found by Kahlweit et al. [16,55]. Thus the penetration rate is greater than predicted by Wagner's model, to the extent necessary to reach a higher solute metal concentration N'_B , where sufficient supersaturation for precipitate nucleation can be achieved.

The distance

$$\Delta X = X_i - X'_i \quad [6.80]$$

represents the spacing between successive nucleation events and is therefore representative of the local precipitate number density, F_N

$$F_N \approx \frac{1}{(\Delta X)^3} = \left(\frac{X_i}{\Delta X} \right)^3 \cdot \frac{1}{X_i^3} \quad [6.81]$$

Kahlweit et al. [16,55] derived the relationships

$$\frac{\Delta X}{X} = \frac{N_o^*}{N_o^{(s)}} \frac{N_B^{(o)} - N'_B}{v N_B^*} = \frac{N'_B - N_o^*}{N_o^{(s)}} \frac{N_B^o - N'_B}{N_B^* - N'_B} = \frac{v(N_B^{(o)} - N'_B)(N_B^* - N'_B)}{\phi N_o^{(s)}(N_B^{(o)} - N_o^*)} \quad [6.82]$$

from which it follows that for D_o , D_B and $N_o^*(B_B^*)^v$ independent of X and $N_o^{(s)}$, then $(N_o^{(s)} \Delta X / X_i)$ is also independent of X_i and $N_o^{(s)}$. Eq. [6.81] can therefore be rewritten as

$$F_N = k \left(N_o^{(s)} \right)^3 / X_i^3 \quad [6.83]$$

where the constant k is a function of $D_o/D_B, N_B^{(o)}, K_{sp}$ and $N_o^*(N_B^*)^v$. The last is unknown but is assumed to be constant. It is then predicted from Eq. [6.83] that under fixed reaction conditions, F_N is proportional to $(N_o^{(s)})^3$, ie,

$$F_N(X_i) = \text{const. } p_{O_2}^{\frac{3}{2}} \quad [6.84]$$

If, furthermore, K_{sp} is very small, solute enrichment is negligible ($\alpha \approx 1$) and the precipitates are spherical, their radius, r , is given by

$$F_N \frac{4\pi r^3}{3} = V_{ox} N_B^{(o)} \quad [6.85]$$

which upon substitution from Eq. [6.83] yields

$$r = \left(\frac{V_{ox} N_B^{(o)}}{4\pi k} \right)^{\frac{1}{3}} \frac{X_i}{N_o^{(s)}} \quad [6.86]$$

Bohm and Kahlweit [16] tested these predictions using internal oxidation of a dilute Ag-Cd alloy at 850°C and confirmed that $F_N(CdO)$ decreased with X_i^3 and increased with $(N_o^{(s)})^3$. However, the assumption is that K_{sp} is very small, and hence $f_{BO} \neq f(x)$ is frequently incorrect. The predictions of Eqs [6.83] and [6.86] will not be obeyed in such cases. An example of this situation is shown in Fig. 6.25, where f_{BO} decreases sharply with increasing depth. Particle size also increases with depth but not in accord with [6.86]. Numerical evaluations by Gesmundo et al. [57] have shown that $k_p^{(i)}$ is quite sensitive to the critical degree of supersaturation required for nucleation when K_{sp} is large. However, in the case of low K_{sp} values considered by Wagner, the predicted values of $k_p^{(i)}$ are essentially unaffected.

Rhines [4] pointed out that the more stable the oxide, the easier the nucleation (see Eq. [6.71]) and the greater the number of precipitates which result. Whilst this may be correct for very dilute alloys, where metal diffusion is slow, it is clearly not a useful generalisation in the cases shown in Figs 6.4 and 6.7. These cellular growth morphologies are found for both a low K_{sp} precipitate (Al_2O_3) and high K_{sp} carbides and nitrides. Indeed, the Kahlweit theory of repeated supersaturation and new precipitate nucleation is clearly inapplicable to these cases where the growth of existing needles or platelet-shaped precipitates is the dominant process, and nucleation is no longer important. As already noted, these morphologies can lead to faster alloy penetration by facilitating oxidant diffusion. The reasons for their development are therefore of interest.

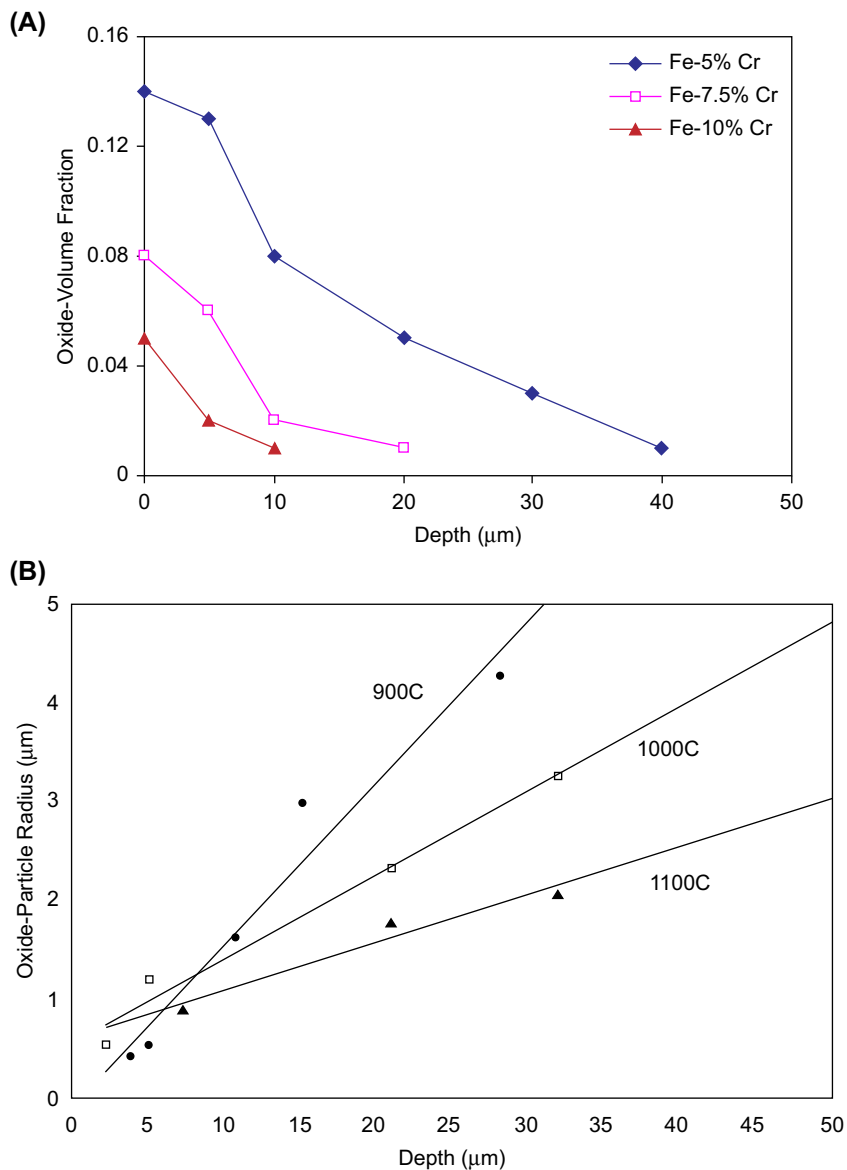


FIGURE 6.25 Internal oxide (A) volume fraction and (B) particle radius in Fe-5Cr at 1000°C. Published with permission from O. Ahmed, D.J. Young, in: M.J. McNallan, E.J. Opila, T. Maruyama and T. Narita (Eds.), *High Temperature Corrosion and Materials Chemistry II*, The Electrochemical Society, Inc., Pennington, NJ (2000), 77, The Electrochemical Society.

6.8 CELLULAR PRECIPITATION MORPHOLOGIES

The application of classical nucleation theory to internal oxidation developed by Kahlweit et al. [16,55,56] assumes that the extent of precipitate growth is limited by the local supply of reacting solute metal. Since this is usually a relatively slow process, it would seem to be a reasonably good assumption. Nonetheless, the growth of rods or laths of Al_2O_3 , Cr_2N and Cr_{23}C_6 has been found to continue across virtually the complete internal precipitation zone. Other examples of these morphologies include MoS_2 precipitates in internally sulfidised Ni-Mo alloys [58], Al_2O_3 in ferritic iron [13], In_2O_3 in Ag-In alloys [59], TiO_2 in Co-Ti alloys [60], Cr_2N in binary Ni-Cr alloys [61] and various commercial heat-resisting alloys [62,63] and Cr_{23}C_6 in a variety of ferritic and austenitic alloys [10,23,64–66]. The example of Cr_2N lamellar precipitate growth in austenite is now investigated.

A low magnification image of the internal nitridation zone is shown in Fig. 6.4, and a high magnification image of the precipitation front in Fig. 6.26 reveals that a grain boundary had developed at the reaction front. Analysis by selected area diffraction (SAD) showed that the precipitates were Cr_2N and the matrix austenite. Their orientation relationship (Fig. 6.26B) was found to be

$$[\bar{1} \bar{2} 10]_{\text{Cr}_2\text{N}} \parallel [\bar{1} 1 \bar{2}]_{\gamma} : (0002)_{\text{Cr}_2\text{N}} \parallel (111)_{\gamma} \quad [6.87]$$

The same orientation relationship was found throughout the precipitation zone, and at all reaction times. The parallel orientations of the Cr_2N lamellae

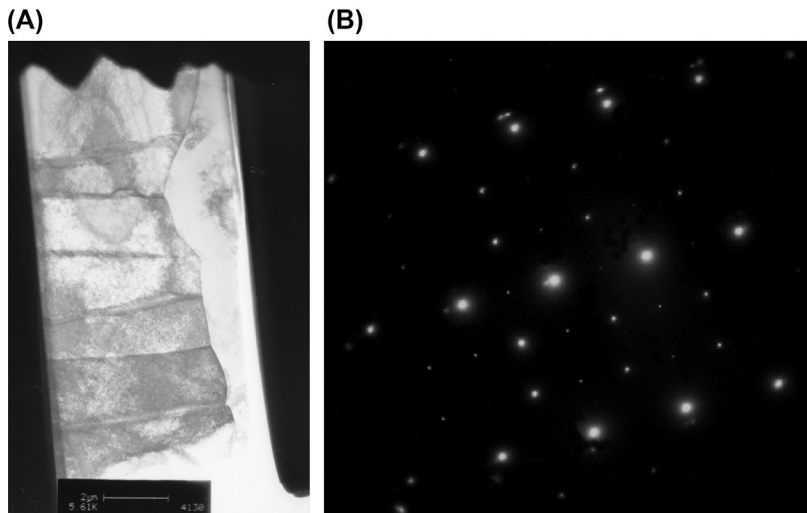


FIGURE 6.26 Internal nitridation reaction front in Fe-25Cr-20Ni at 1000°C: (A) bright field TEM and (B) SAD pattern near precipitation front: large, bright spots show $[112]$ zone axis of austenite, and small spots show $[11\bar{2}0]$ zone axis of Cr_2N .

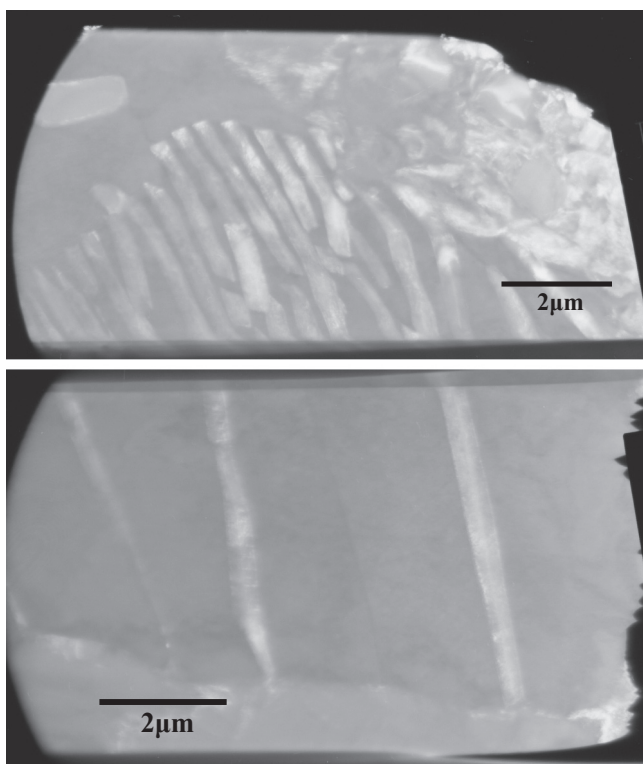


FIGURE 6.27 Dark field images of Cr_2N precipitates 5 μm below the alloy surface and at the precipitation front ($X_i = 60 \mu\text{m}$) in Fe-25Cr-20Ni after 90 min at 1000°C.

are clear in the dark field images of Fig. 6.27. The parent austenite grain ahead of the precipitation front and the product austenite grain behind the front were of different orientations. Neither the Cr_2N nor the reacted austenite grain had rational orientation relationships with the parent grain.

Chemical microanalysis performed by energy dispersive spectrometry (EDAX) in the TEM yielded results for the reaction front. A scan across the unreacted–reacted austenite grain boundary (Fig. 6.28) showed a small step function decrease in N_{Cr} at the boundary. A scan in the orthogonal direction, parallel to the reaction front, revealed a completely flat profile between precipitates.

The morphology, structure and compositional variations observed at the nitridation front are characteristic of the cellular ‘discontinuous precipitation’ reaction. Such a reaction is characterised by lamellar or rod-shaped precipitates growing with an orientation relationship to their matrix, a high angle boundary at the precipitate growth front where the unreacted alloy and reacted matrix are the same phase but are differently oriented and a step function or

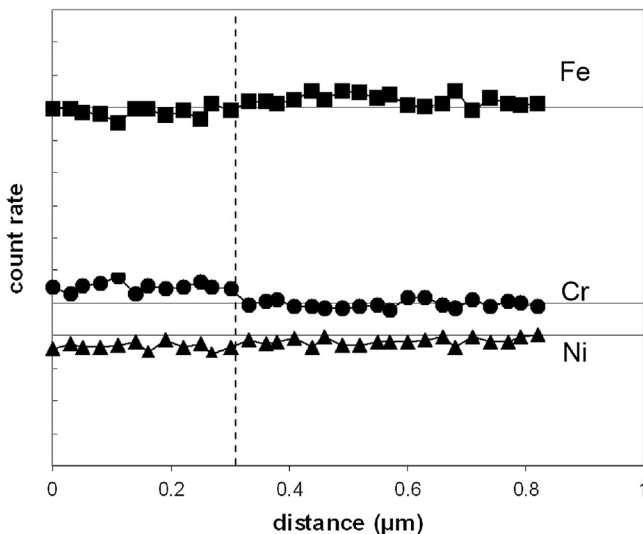


FIGURE 6.28 EDAX analysis across the unreacted-reacted austenite grain boundary at the internal nitridation front of Fig. 6.26.

'discontinuous' change in composition at the precipitation front [67]. In a closed system, it would be written as

$$\gamma = \gamma^D + P \quad [6.88]$$

with γ indicating parent austenite, γ^D the chromium-depleted matrix and P the precipitate. For the internal nitridation reaction, we write



and show the mass transport processes schematically in Fig. 6.29. Nitrogen is transported from the alloy surface to the discontinuous precipitation front by a mixture of lattice diffusion through the matrix phase and diffusion along the interfaces between the lamellae and matrix. The γ/γ^D high angle boundary provides a pathway for rapid lateral transport of chromium, allowing it to segregate to the advancing Cr_2N lamellae tips, and for the rejection of iron and nickel from the nitride.

In this situation, the rate of precipitate penetration into the alloy is controlled by the nitrogen diffusion rate, but the spacing of the precipitate lamellae is controlled by chromium diffusion at the precipitation front. If the latter process is one of grain boundary diffusion, then [68,69]

$$\frac{dX_i}{dt} = \frac{kD_{Cr,i}}{S^2} \quad [6.90]$$

where k is a constant, $D_{Cr,i}$ is the diffusion coefficient at the γ/γ^D boundary and S is the cellular dimension defined in Fig. 6.29. The form of Eq. [6.90]

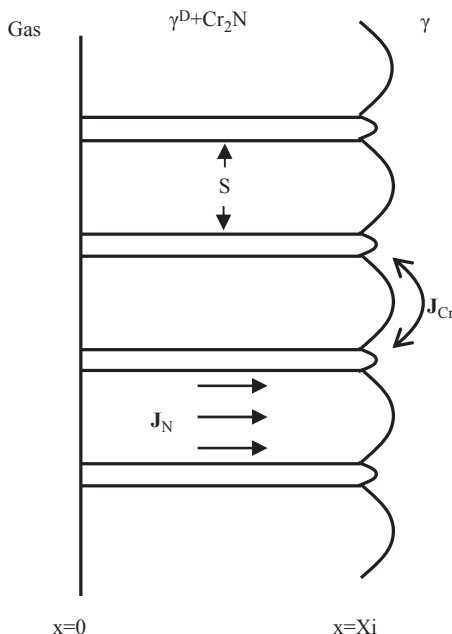


FIGURE 6.29 Mass transport processes involved in discontinuous precipitation of Cr_2N during internal nitridation of austenite.

reflects the fact that the rate at which the precipitates advance must balance the rate at which chromium is delivered to their tips ($\sim D_{\text{Cr},i}/S$), together with the fact the total precipitate-matrix surface area created (which is proportional to $1/S$) is minimised.

Precipitate lamellae spacings developed during internal nitridation of austenite are shown in Fig. 6.30. The spacing at a given depth remains constant with time, and the spacing at the moving reaction front increases with depth. Calculating the reaction front speed from $dX_i/dt = k_p^{(i)}/X_i$ and the measured [70] value of $k_p^{(i)}$, the spacing data of Fig. 6.30 are plotted according to Eq. [6.90] in Fig. 6.31. Agreement with the discontinuous precipitation theory is seen to be good.

There remain the questions as to why and how the discontinuous precipitation morphology was adopted by the reacting system. Two key factors are involved: the existence of a precipitate-matrix orientation relationship, which can reduce surface energy, and the low stability of Cr_2N with the consequently small driving force for precipitate nucleation at low $N_{\text{N}}^{(s)}$ levels.

The precipitates are constrained in their growth direction by the availability of chromium and nitrogen. The average direction normal to the alloy surface

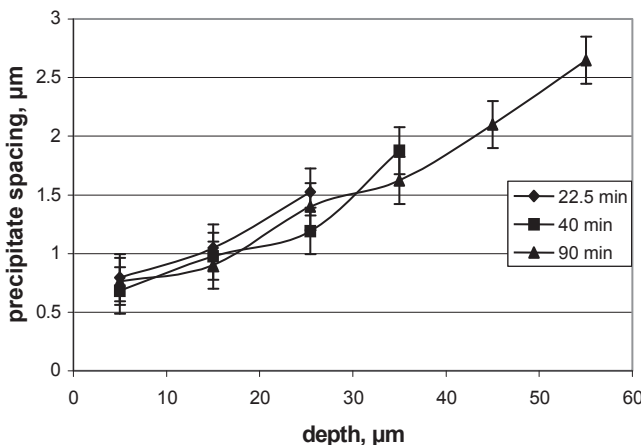


FIGURE 6.30 Variation of nitride spacing with position within precipitation zone at different reaction times for Fe-25Cr-20Ni at 1000°C.

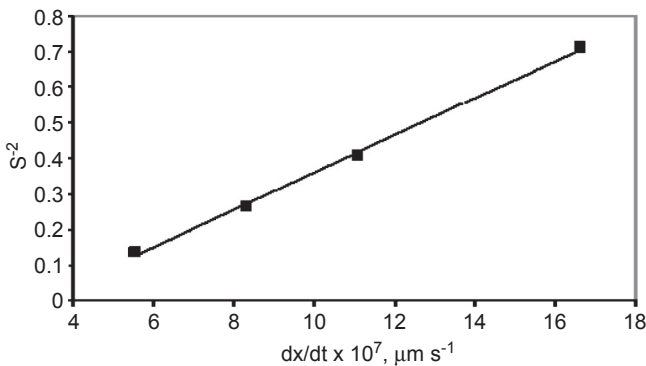


FIGURE 6.31 Test of discontinuous precipitation Eq. [6.90] for internal nitridation of Fe-25Cr-20Ni at 1000°C.

minimises the nitrogen diffusion distance to where immobile chromium remains as yet unreacted. Thus a lamellar morphology is kinetically favourable but creates a large internal surface area. The Cr₂N-austenite system is able to reduce the surface energy by adopting a largely coherent precipitate-matrix orientation relationship. However, to accommodate both the preferred precipitate growth direction and the energetically favourable orientation relationship, the austenite matrix needs to adopt the appropriate orientation, which will, in general, be different from that of the parent grain. For this reason, the austenite undergoes reorientation at the reaction front, a process facilitated by the diffusion occurring along this high angle boundary.

Clearly the cellular precipitation process is self-sustaining. However, it is of enduring stability only because new precipitates do not nucleate ahead of

the reaction front. The primary reason for this is the low stability of Cr₂N and its high solubility product (Table 6.5). The free energy barrier to nucleation (Eq. [6.71]) is consequently high, and the nitrogen supersaturation necessary to overcome it is not achievable when growth of the existing lamellae is supported by accelerated chromium diffusion to their tips.

A similar situation arises during lamellar Cr₂₃C₆ growth, as discussed in Chapter 9. On the other hand, the formation of alumina rod and lath shaped precipitates is apparently different. As seen in Fig. 6.7, and even more clearly in Fig. 6.32, the precipitates extend across the width of the internal oxidation zone. However, no grain boundary develops in the metal phase at the reaction front, no orientation relationship is established between the Al₂O₃ and the metal and it must be concluded that the discontinuous precipitation mechanism is not in effect. The reasons for the formation of elongated Al₂O₃ precipitates have not been clearly established, although it is reasonable to speculate [60] that rapid diffusion of precipitating metal to the growing particles prevents nucleation of new ones. In that case, it would be expected that varying temperature and p_{O_2} , so as to alter D_o/D_{Al} , would affect the precipitate morphology. This question appears not to have been adequately investigated.

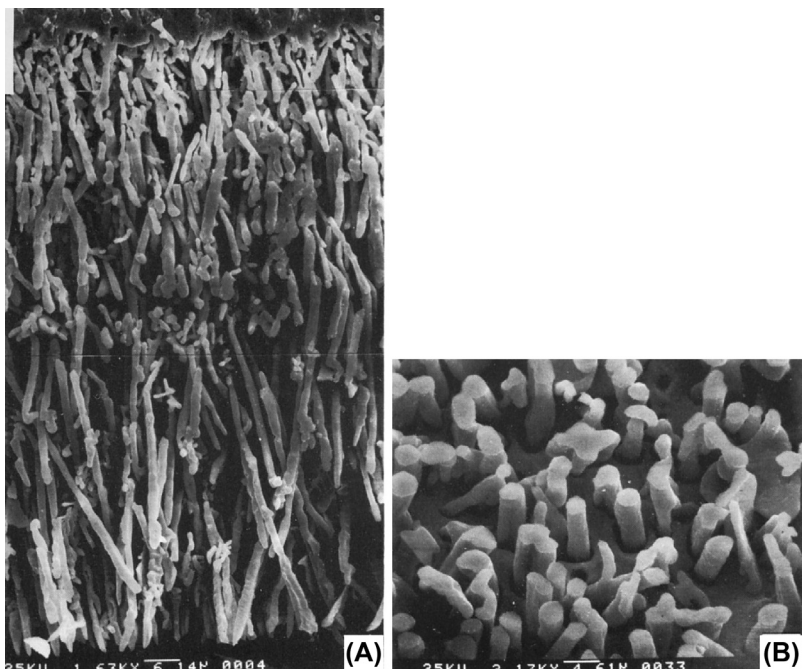


FIGURE 6.32 Rod-shaped oxide precipitates formed during internal oxidation of Ni-4Al as revealed by SEM examination of deep etched specimens. *With kind permission from H. Hindam, D.P. Whittle, J. Mater. Sci. 18 (1983) 1389, Springer Science and Business Media.*

6.9 MULTIPLE INTERNAL PRECIPITATES

We consider first the case where the solute metal forms two different precipitates corresponding to different oxidation states. The example of internal carburisation-forming zones of Cr_7C_3 and Cr_{23}C_6 precipitates is illustrated in Fig. 6.6. Another common example is the formation of a spinel phase together with either Cr_2O_3 or Al_2O_3 . In all such cases, the existence of different precipitate zones is a consequence of the gradient in oxidant potential between its maximum at the alloy surface and minimum in the alloy interior. A diffusion path for the internal oxidation of a Ni-Al alloy is shown in Fig. 6.33, drawn on the basis that $D_0 \gg D_{\text{Al}}$. The two reaction fronts within the internal precipitation zone correspond to the reactions

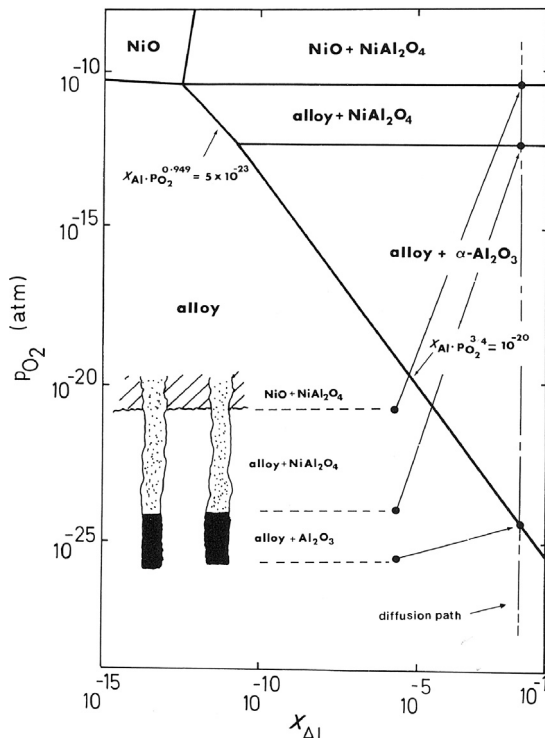
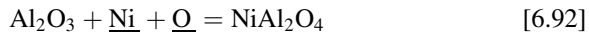
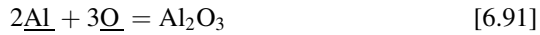


FIGURE 6.33 Diffusion path for internal oxidation of dilute Ni-Al at 1000°C. With kind permission from H. Hindam, D.P. Whittle, J. Mater. Sci. 18 (1983) 1389, Springer Science and Business Media.

In the aluminium alloy case, precipitate growth predominates over nucleation, and the amount of oxygen supersaturation required at each interface is presumably small.

The general situation of two precipitate zones was described by Meijering [11] on the assumptions that B was immobile, both precipitates had very low K_{sp} values and that the interface between the two zones was sharp, ie, reaction [6.92] or its equivalent instantaneously achieved equilibrium. The diffusion model is shown schematically in Fig. 6.34. The intermediate reaction front where BO_{v1} is further oxidised to BO_{v2} is located at $x = X_I$. The oxidant concentration at this point is denoted by N_O^I . Using the linear concentration gradient approximation in Fick's law (as in Eq. [6.7]) and utilising the mass balances at the two reaction fronts (as in Eq. 6.8]), Meijering wrote

$$\frac{D_o N_O^I}{X_i - X_I} = v_1 N_B^{(o)} \frac{dX_i}{dt} \quad [6.93]$$

and

$$\frac{D_o (N_O^{(s)} - N_O^I)}{X_I} = v_1 N_B^{(o)} \frac{dX_i}{dt} + (v_2 - v_1) N_B^o \frac{dX_I}{dt} \quad [6.94]$$

It is seen that both zones widen according to parabolic kinetics. The analysis leads to the expression for total penetration

$$X_i^2 = \frac{2 D_o N_O^{(s)}}{v_{\text{eff}} N_B} t \quad [6.95]$$

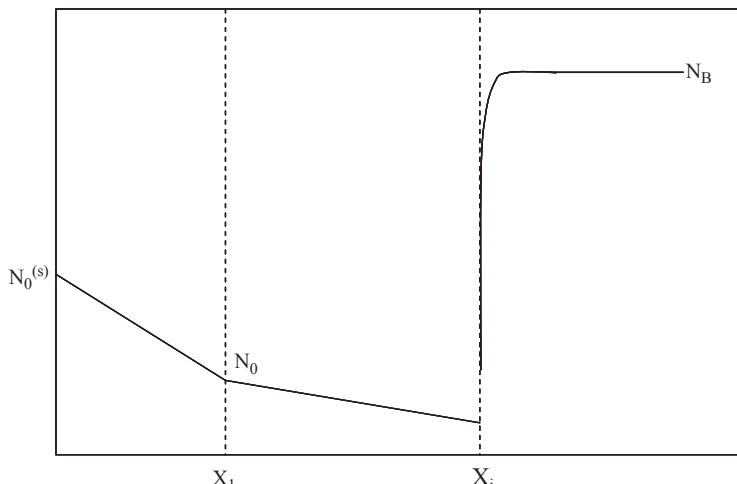


FIGURE 6.34 Reactant concentration profiles when two precipitate zones form from a single oxidant and one solute metal.

which is seen to be equivalent to Eqs [6.1] and [6.11]. The effective stoichiometric coefficient is given by

$$v_{\text{eff}} = \left[\frac{v_1}{m} \left(1 - \frac{(1 + 4m(1-m)(v_2 - v_1)/v_1)^{\frac{1}{2}} - 1}{2m(v_2 - v_1)/v_1} \right) \right] \quad [6.96]$$

where $m = N_o^I/N_o^{(s)}$. Whilst this analysis can in principle predict the ratio X_I/X_i , this requires a knowledge of N_o^I , which is indeterminate within the formalism. The practical utility of Eq. [6.94] lies in its application when $X_I/X_i, v_1$ and v_2 are all known, and penetration kinetics are used to deduce the permeability $N_o^{(s)}D_o$.

A somewhat similar situation can arise in the internal oxidation of ternary alloys, if two components are reactive as shown schematically in Fig. 6.35. Studies of this sort date back to the pioneering work of Rhines [4] on copper alloys containing tin or zinc as well as one of aluminium, beryllium or silicon. He produced two internal oxidation zones, with the inner one containing the more stable oxide. The example of simultaneous internal oxidation of chromium and aluminium in a nickel alloy is shown in Fig. 6.8.

A more sophisticated treatment of the simultaneous internal oxidation of two solute metals has been provided by Niu and Gesmundo [71]. However, it too fails to provide a prediction of where the reaction front for the less stable precipitate will be located. As a result, the theory cannot predict the degree of enrichment in the near-surface zone, because this is supported by diffusion of the less reactive solute metal through the inner precipitation zone. The theory was applied with qualitative success to the internal oxidation of aluminium and silicon in Ni-Si-Al, using the approximation that the intermediate SiO_2 precipitation front coincided with that of Al_2O_3 , thereby removing the uncertainty. However, Yi et al. [72] showed clearly that Al_2O_3 was precipitated at greater depth than SiO_2 .

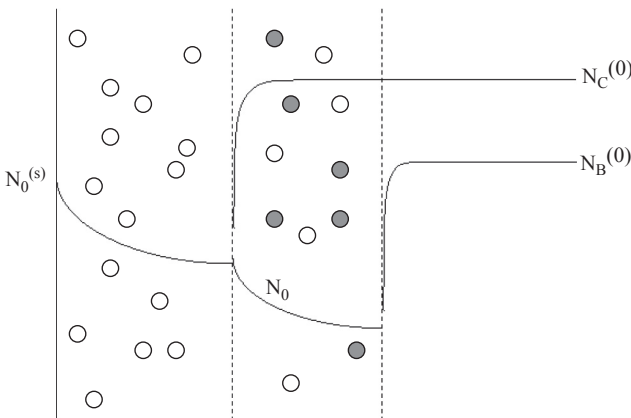


FIGURE 6.35 Simultaneous internal oxidation of two solute metals in ternary alloy.

Another example of multiple internal precipitation zones arises when a dilute alloy is simultaneously attacked by two or more different oxidants. This situation also was first analysed by Meijering [11] and is shown schematically in Fig. 6.36. The oxidant forming the less stable precipitate under reaction conditions will be found in the deeper reaction zone, if it is formed. The reason for this is that the more stable precipitate forms at or near the surface if the reaction, for example,

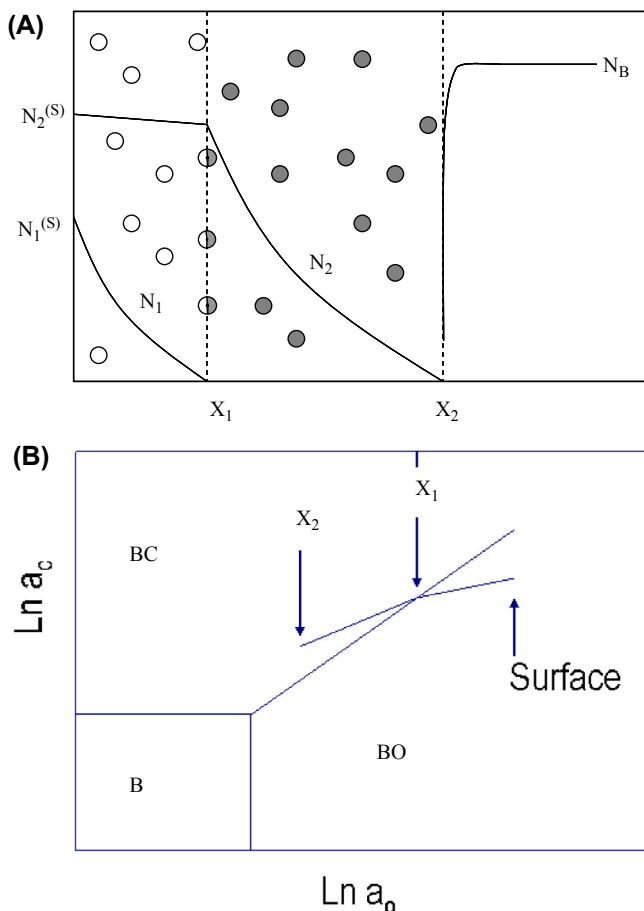
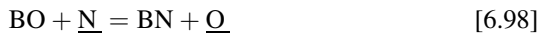


FIGURE 6.36 (A) Concentration profiles for simultaneous internal attack on alloy AB by two oxidants, assuming essentially immobile B. (B) Corresponding diffusion path for the oxidising-carburising case.

is favoured by the gas composition. Beneath the surface, N_{O} decreases with depth, until reaching a low value at the oxide precipitation front. If diffusion of nitrogen through the near-surface oxide precipitation zone is rapid, then N_{N} does not decrease very much, and a position is reached where $N_{\text{N}}/N_{\text{O}}$ exceeds the value necessary for the reaction



where nitride precipitation commences.

The Meijering analysis assumes

- a. neither precipitate significantly affects the inward oxidant diffusion rates;
- b. the less stable precipitate is converted to the more stable one via a displacement reaction involving dissolved oxidant (1);
- c. the displacement reaction goes rapidly to completion at precisely defined oxidant activity values, ie, no intersolubility exists between the two precipitate compounds;
- d. no thermodynamic or kinetic interaction of importance takes place in the solution phase; and
- e. precipitates are extremely stable, and $N_{\text{B}} \cong 0$ throughout the two precipitate zones.

Under these conditions, the two zones grow each according to parabolic kinetics. Meijering further assumed that the alloy solute B is essentially immobile, and no solute enrichment occurs in the precipitation zone. The approximate Meijering treatment leads to the results

$$X_1^2 = 2 \frac{D_1 N_1^{(\text{s})}}{v_1 N_{\text{B}}^{(\text{o})}} t \quad [6.99]$$

$$X_2^2 = 2 \left(\frac{D_1 N_1^{(\text{s})}}{v_1 N_{\text{B}}^{(\text{o})}} + \frac{D_2 N_2^{(\text{s})}}{v_2 N_{\text{B}}^{(\text{o})}} \right) t \quad [6.100]$$

These simple forms result from the way in which the intermediate precipitation front at X_1 is treated. The Meijering treatment assumes that the oxidant (2) released at this position by the displacement reaction, which is the reverse of Eq. [6.98], all diffuses inward to extend the inner precipitation zone. Thus if an alloy was first reacted to internally precipitate the less stable compound, eg, BN, and then was exposed to oxygen alone, the advancing oxidation front would displace the internally nitrided zone inwards, but the thickness of the nitride zone would remain constant. In essence, therefore, the innermost precipitation zone is predicted to widen at the same rate, whether or not another precipitation zone develops near the surface.

The formation of two separate precipitation zones in sequence according to thermodynamic stability has been verified [73,74], but kinetic data have become available only recently. When heat-resistant alloys were exposed [75]

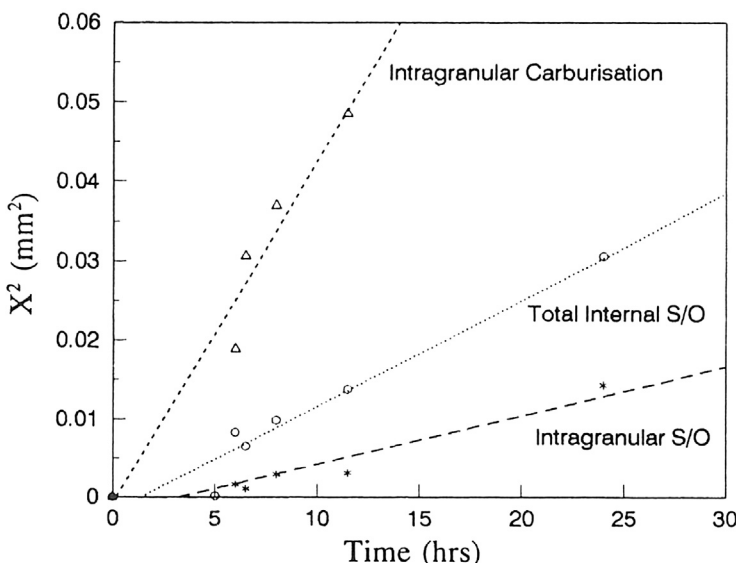
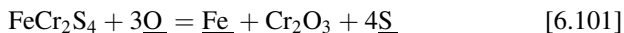


FIGURE 6.37 Internal precipitation zone growth kinetics for 310 stainless steel exposed to CO-CO₂-SO₂-N₂ at 1000°C. With kind permission from D.J. Young, S. Watson, *Oxid. Met.* 44 (1995) 239, Springer Science and Business Media.

to two-component (CO/CO₂) or three-component (CO/CO₂/SO₂) gases, they developed discrete internal precipitation zones which each grew according to parabolic kinetics, as shown in Fig. 6.37. However, the assumption of a single precipitate species in each zone, whilst appropriate for binary alloys, was found to be inapplicable to these multicomponent materials. The observation of chromium rich oxide and sulphide precipitates in the same zone was common. The sulphide also contained iron. Approximating this compound as a thiospinel, one can write



for precipitate coexistence. Since a_{Fe} can vary within the matrix of a multicomponent alloy, a_s and a_o are independent, and the two-precipitate zone can be both thermodynamically and kinetically stable. Unfortunately, the experiments behind the data of Fig. 6.37 also produced external scales, boundary conditions were uncertain and further analysis is not possible.

Gesmundo and Niu [76] have relaxed the requirement that $D_B \approx 0$ and have avoided other approximations in the Meijering treatment. However, they retained the assumption that K_{sp} in both precipitate zones is very small, and consequently, $N_B \approx 0$. Enrichment of precipitated element B in the internal reaction zones was found to affect the rates at which the oxidants penetrated deeper into the alloy. However, predictions made for the simultaneous internal carburisation and oxidation of Ni-3.9w/o Cr in CO/CO₂ at 821°C were in

poor agreement with the experimental data of Copson et al. [77,78]. Whilst the basic data used in the calculation $(N_o^{(s)}, D_o, N_c^{(s)}, D_c, D_{Cr})$ were of high quality, it had been measured at high temperatures. Extrapolation to low temperatures, such as the 821°C used by Hopkinson and Copson, is always somewhat questionable for diffusion coefficients in view of the increasing importance of boundary and dislocation mechanisms.

The simultaneous carburisation and oxidation of chromium-bearing alloys is an important technical problem, leading to a form of failure known as ‘green rot’ [79]. The name comes from the green colouration of fracture surfaces in the embrittled material resulting from this form of internal attack. The general reaction morphology is shown in Fig. 6.38 for a Type 304 stainless steel (Fe-18Cr-8Ni base) exposed at 700°C to a CO/CO₂ mixture corresponding to $p_{O_2} = 10^{-23}$ atm and a supersaturated carbon activity of 7. An external scale was formed but was repeatedly disrupted and spalled by regular temperature cycling. As seen in the micrograph, two internal precipitation zones were formed: oxides beneath the surface and carbides at greater depths. The oxide zone actually consisted of two regions: spinel nearest the surface, and Cr₂O₃ further in.

The practical effect of the carburisation is profound. In the absence of carbon, this alloy would form an external oxide scale rather than undergoing internal oxidation (see Section 6.11). Because carbon permeability in the alloy is so high ($D_c N_c^s \approx 6 \times 10^{-11} \text{ cm}^2 \text{ s}^{-1}$ at 700°C), internal carburisation is rapid, removing much of the chromium from solution. The precipitated chromium is immobilised, and is therefore unavailable to form an external oxide scale. Instead, the carbides are oxidised *in situ*, just as proposed by

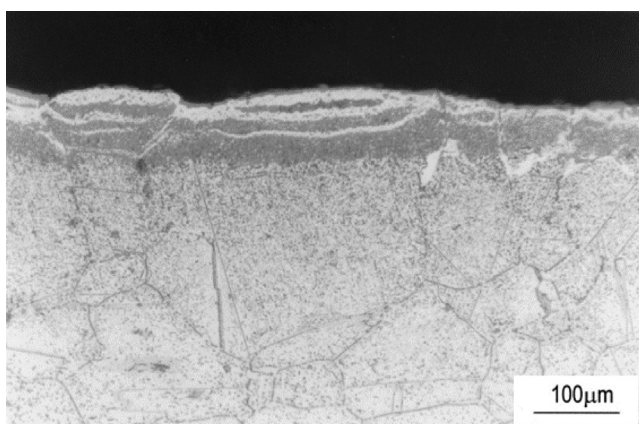


FIGURE 6.38 Internal carburisation and oxidation of a 304 stainless steel exposed to CO-CO₂-Ar at 700°C. Reprinted from with permission from M. Hänsel, C.A. Boddington, D.J. Young, Corros. Sci. 45 (2003) 967, Elsevier.

Meijering. Only in this way could the enormous oxide volume fractions seen in Fig. 6.38 be formed internally. The Cr₂O₃ is responsible for the green colour and the expressive term, green rot.

The carburisation front was found to have penetrated 520 µm in 396 h at 700°C, corresponding to

$$2 \left(\frac{D_o N_o^{(s)}}{1.5 N_{Cr}^{(o)}} + \frac{D_c N_c^{(s)}}{0.344 N_{Cr}^{(o)}} \right) = 1.9 \times 10^{-9} \text{ cm}^2 \text{ s}^{-1}$$

according to [6.100]. Permeability data are not available for such a low temperature, so high temperature data were extrapolated, yielding $D_o N_o^{(s)} / 1.5 N_{Cr}^{(o)} = 2 \times 10^{-18} \text{ cm}^2 \text{ s}^{-1}$ and $D_c N_c^{(s)} / 0.344 N_{Cr}^{(o)} = 9 \times 10^{-10} \text{ cm}^2 \text{ s}^{-1}$. Clearly the oxygen permeability data are not applicable to the observed internal oxidation rates, but the carbon permeability is roughly in accord with the experimental carburisation depth.

Alloys containing two or more reactive solute metals exposed to mixed oxidant gases can form very complex internal precipitation zones. Oxidation in air under thermal cyclic conditions (which remove scale and allow internal attack) led to the internal formation of nitrides and oxides of both aluminium and chromium [81] in Ni-Al-Cr alloys. As expected, the nitrides were located deeper within the reaction zone (Fig. 6.39), reflecting their lower stability and the high nitrogen permeability. The sequence of chromium and aluminium nitrides was, however, unexpected. It can be understood in terms of thermodynamic interactions within the matrix phase, as is discussed in Section 6.10.

Internal penetration rates were rapid, in the range $k_p^{(i)} = 1.5 - 5.1 \times 10^{-10} \text{ cm}^2 \text{ s}^{-1}$ at 1100°C for a range of alloy compositions. The applicability of Eq. [6.100] was tested using oxygen and nitrogen permeability data. For $N_{Al} = 0.2$, $N_o^{(s)} D_o / 1.5 N_{Al}^{(o)} = 3 \times 10^{-10} \text{ cm}^2 \text{ s}^{-1}$ and $N_N^{(s)} D_N / N_{Al}^{(o)} = 5 \times 10^{-10} \text{ cm}^2 \text{ s}^{-1}$. The overall rate constant predicted from Eq. [6.100] to be $5.3 \times 10^{-10} \text{ cm}^2 \text{ s}^{-1}$ was in satisfactory agreement with the experimental results.

The kinetic models for internal attack by multiple oxidants have a critical shortcoming. Both the approximate Meijering model [11] and the more accurate Gesmundo and Niu [76] description treat the reactant metal B as being at a negligible matrix concentration throughout the multiple precipitation zones. Whilst this might be a reasonable approximation for oxide formation, it is nowhere near correct for carbides or nitrides (Table 6.5). A large concentration of chromium remains in the matrix of the inner carbide or nitride zone, and will react with inwardly diffusion oxygen when it arrives. Thus the description of the mass balance at the intermediate interface X_1 (Fig. 6.36), solely in terms of a reaction such as Eq. [6.98], is in considerable error. This is illustrated in Fig. 6.40 for the case of internal nitridation followed

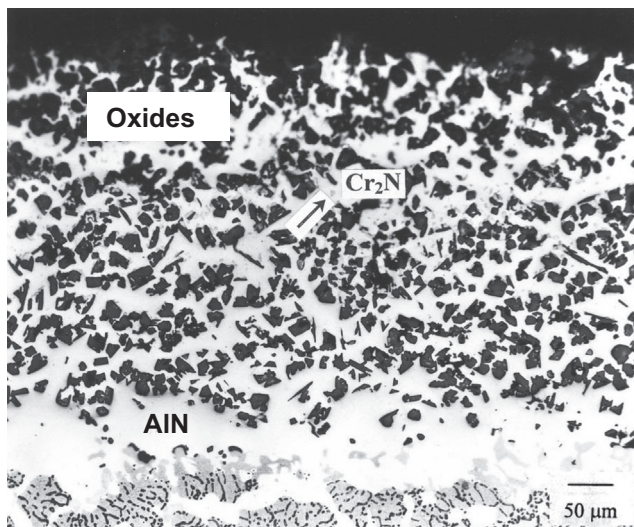


FIGURE 6.39 Simultaneous internal nitridation and oxidation of Ni-Cr-Al exposed to air for 160 one-hour cycles at 1100°C.

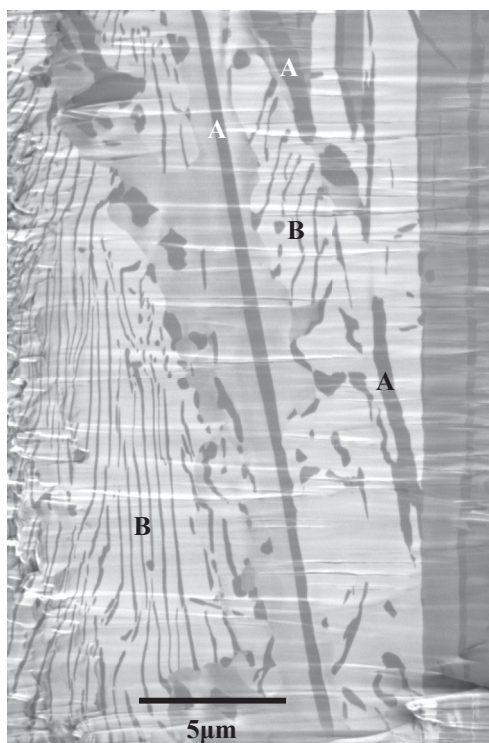
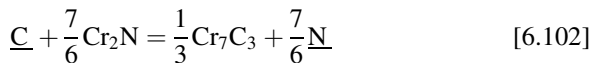


FIGURE 6.40 Sequential internal nitridation followed by carburisation of a Ni-25Cr-20Ni alloy at 1000°C: A, prior nitrides carburised in situ; B, secondary carbides.

by carburisation. The arrival of carbon has converted the large lamellar prior nitrides in situ to carbide, as expected. In addition, however, it has reacted with matrix chromium to form additional fine carbides. A further complication is the appearance in this zone of CrN, a phase which is unstable at the ambient nitrogen pressure employed. The reason [82] is likely the release of nitrogen via the reaction



The saturation level $N_{\text{N}}^{(\text{s})}$ corresponds in this reaction to an equilibrium value of $N_{\text{c}} = 1.4 \times 10^{-3}$. However, much higher levels of N_{c} are available from carbon dissolution, up to about 0.06, leading to higher (supersaturated) N_{N} values according to Eq. [6.102]. Under these circumstances CrN is stabilised. Given all of these complexities, the kinetic theory cannot be expected to provide any better than order of magnitude predictions. The further approximation in the Meijering theory that $N_{\text{O}}^{\text{I}} = 0$ is an additional source of error in the case of carburisation-oxidation reactions.

6.10 SOLUTE INTERACTIONS IN THE PRECIPITATION ZONE

We have assumed so far that the various alloy solutes, oxidants and reacting metals behave in an ideal fashion, having no effect on each other's thermodynamic activity or diffusion. Given that the oxidant and solute species interact chemically to the extent of forming a precipitate, the supposition is seen to be improbable. Nonetheless, as seen earlier in this chapter, the diffusion theories of Rhines, Wagner and Meijering have proven remarkably successful in providing at least semiquantitative descriptions of internal penetration rates in many cases. The questions of interest therefore concern how large the solute interactions are and when they become important.

Gesmundo and Niu [83] have considered the general quaternary system A-B-C-O, in which the only oxides possible are the pure binaries. It is supposed that the stability of the oxides increases in the order AO, BO, CO_v , and that the oxygen potential is sufficient to oxidise only C. Assuming that $K_{\text{sp}}(\text{CO}_v) \ll 1$, the situation is one of oxygen dissolving in and diffusing through a single-phase A-B matrix. The effects of B on oxygen permeability and hence internal oxidation can therefore be investigated. Ternary diffusion interactions were ignored in this analysis, and attention was focused on oxygen solubility. The model originally proposed by Alcock and Richardson [84] for oxygen solubility in liquid binary alloys was employed

$$\ln K_s(\text{AB}) = N_A \ln K_s(\text{A}) + N_B \ln K_s(\text{B}) + N_A \ln \gamma_{\text{A}}(\text{AB}) + N_B \ln \gamma_{\text{B}}(\text{AB}) \quad [6.103]$$

where $K_s(i)$ is the Sievert's constant (Eq. [2.71]) for oxygen in the indicated solvent, and $\gamma_{\text{A}}(\text{AB})$ and $\gamma_{\text{B}}(\text{AB})$ are the metal activity coefficients in the

binary alloys. Approximate ideality was assumed for the substitutional alloy solution, yielding the simplified result

$$\ln K_s(AB) = N_A \ln K_s(A) + N_B \ln K_s(B) \quad [6.104]$$

and the oxygen solubility in the alloy is given by

$$N_o^s(AB) = K_s(AB) p_{O_2}^{\frac{1}{2}} \quad [6.105]$$

The oxygen diffusion coefficient also varies with AB composition. The original model of Park and Altstetter [85] for oxygen dissolution in binary alloys

$$D_o(AB) = D_o(A) \frac{\gamma_o(AB)}{\gamma_o(A)} \quad [6.106]$$

was examined. However, because $K_s = 1/\gamma_o$, this description leads to the unacceptable result

$$D_o(B) = D_o(A) \frac{K_s(A)}{K_s(B)} \quad [6.107]$$

To avoid this difficulty, the empirical description

$$D_o(AB) = D_o(A) \left(\frac{D_o(B)}{D_o(A)} \right)^{N_B} \quad [6.108]$$

was adopted.

The solutions to the diffusion equation for O within the precipitation zone and C in the alloy ahead of the precipitation front are the same as Eqs [6.17]–[6.27]. Application of this model for alloy interaction effects on oxygen permeabilities to the systems Cu-Al, Ni-Al and Cu-Ni-Al led to the results shown in Table 6.7. Whilst the model successfully predicted that adding nickel to Cu-Al would reduce greatly the extent of internal oxidation, it overestimated

TABLE 6.7 Estimate [83] of $k_p^{(i)}$ ($\text{cm}^2 \text{s}^{-1}$) From Eq. [6.108] for Internal Oxidation at 800°C in Rhines Packs

| | Measured | Calculated |
|--------------------|-----------------------|-----------------------|
| Cu-0.72Al | 2.0×10^{-9} | 1.3×10^{-8} |
| Ni-0.54Al | 1.4×10^{-10} | 1.4×10^{-11} |
| Cu-10.16 Ni-0.76Al | 2.9×10^{-11} | 4.8×10^{-12} |
| Cu-20.11 Ni-0.79Al | 2.5×10^{-11} | 6.3×10^{-12} |
| Cu-30.07 Ni-0.80Al | 1.5×10^{-11} | 8.1×10^{-12} |

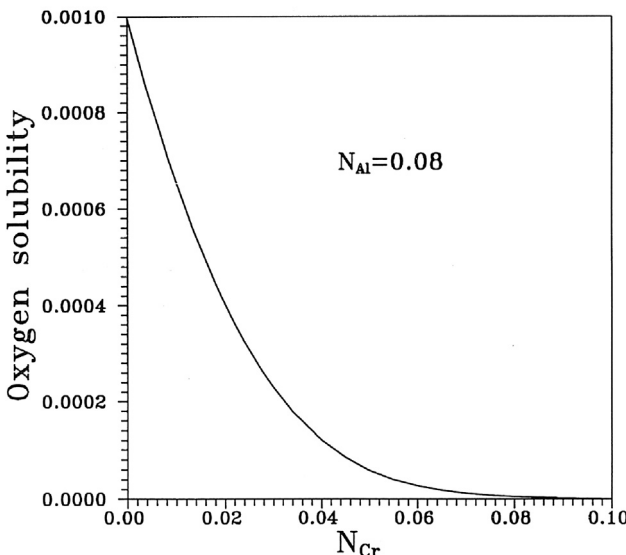


FIGURE 6.41 Oxygen solubility in Ni-Cr-Al as a function of $N_{Cr}^{(o)}$ at 1200°C. With kind permission from S.W. Guan, W.W. Smeltzer, *Oxid. Met.* 42 (1994) 375, Springer Science and Business Media.

the size of the effect and was unsuccessful in relating rates to nickel concentrations.

A much more detailed analysis was undertaken by Guan and Smeltzer [86], who examined the Ni-Cr-Al system. Their approach was based on the use of Wagner's formalism (Eq. [2.68]) for solute interactions to evaluate $N_o^{(s)}$ (Ni-Cr) and a full solution of the diffusion equations, including cross-effects. Results for the variation of oxygen solubility with $N_{Cr}^{(o)}$ are shown in Fig. 6.41. Such large changes in $N_o^{(s)}$ would be expected to affect the rate of internal aluminium oxidation and perhaps limit the possibility of it occurring at all. The results of this calculation are examined in Section 7.4.

A final example of the importance of solute interactions is provided by the internal nitridation of Ni-Cr-Ti alloys [87]. Reaction rates at nitrogen potentials high enough to react with titanium but not chromium were found to increase with $N_{Cr}^{(o)}$. The effect was shown to be due to the Cr-N thermodynamic interaction which increased $N_N^{(s)}$.

6.11 TRANSITION FROM INTERNAL TO EXTERNAL OXIDATION

As is discussed in Chapter 5, if an alloy contains a sufficient concentration of its most reactive component, then the metal can form a protective external

scale. Conversely, if the component is dilute, and no other alloy component is oxidised, then internal oxidation results, destroying the alloy. We now consider what concentration of solute metal is necessary to ensure external rather than internal oxide formation.

Darken [88] recognised that the volume fraction of internally precipitated oxide would affect the reaction, and that internal oxidation could only occur up to a maximum value of f_{BO} , and hence $N_{\text{B}}^{(o)}$. Wagner [8] proposed that a transition from internal to exclusive external oxidation would occur when $N_{\text{B}}^{(o)}$ was increased to a critical value at which the internally precipitated particles reduced the oxygen flux to a sufficient extent. Since the oxide is essentially impermeable to oxygen, diffusion is restricted to the metal channels between precipitate, so that the average flux is lowered. This slows the rate at which the supersaturation needed for new precipitate nucleation can be achieved, and the outward flux of component B is then of greater relative importance. If $N_{\text{B}}^{(o)}$ is high enough to sustain a sufficient flux for the continued growth of precipitates, their enlargement leads to continuous oxide layer formation. The mole fraction of internal oxide is found by definition (Eq. [6.29]) to be

$$f_{\text{BO}} = \alpha N_{\text{B}}^{(o)} \quad [6.109]$$

where α is the enrichment factor calculated from Eq. [6.30]. Under the limiting conditions of Eq. [6.25], where metal solute diffusion is important, the limiting form Eq. [6.31] applies. Recognising that the volume fraction of BO, g_{BO} , is given by

$$g_{\text{BO}} = f_{\text{BO}} \frac{V_{\text{BO}}}{V_{\text{A}}} \quad [6.110]$$

we combine Eqs. [6.31], [6.109] and [6.110] to obtain

$$N_{\text{B}}^{(o)} = \left(g_{\text{BO}} \frac{\pi}{2v} \frac{V_{\text{A}}}{V_{\text{OX}}} \frac{N_{\text{o}}^{(s)} D_{\text{o}}}{D_{\text{B}}} \right)^{\frac{1}{2}} \quad [6.111]$$

If a critical value can be specified for g_{BO} , then the minimum value of $N_{\text{B}}^{(o)}$ for external scale formation can be calculated from Eq. [6.111].

Rapp [89] studied the internal oxidation of Ag-In alloys at 550°C, where Ag_2O is unstable over a wide range of p_{O_2} , the conditions [6.23] were met and $\alpha = 1$. Systematic variation of $N_{\text{In}}^{(o)}$ established that the critical value for scale formation rather than internal oxidation was $f_{\text{InO}_{1.5}} = N_{\text{In}}^{(o)} = 0.15$. This corresponded to an oxide volume fraction, $g_{\text{BO}} = 0.30$. At low p_{O_2} values, where $N_{\text{o}}^{(s)}$ is reduced, the conditions (Eq. [6.25]) are met, and Eq. [6.111] applies. As is seen from this equation, the critical value of $N_{\text{B}}^{(o)}$ varies with $N_{\text{o}}^{(s)}$, and hence

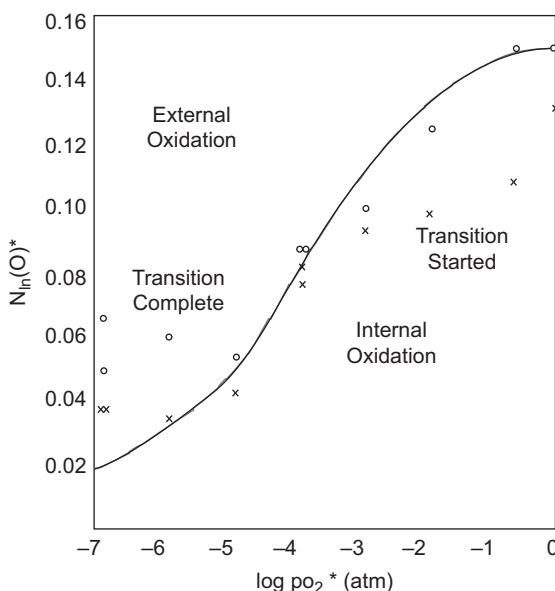


FIGURE 6.42 Transition internal to external oxidation of Ag-In alloys at 550°C. Reprinted from with permission from R.A. Rapp, *Acta Met.* 9 (1961) 730, Elsevier.

with p_{O_2} . Rapp determined metallographically the levels of $N_{In}^{(o)}$ required for scale formation at different oxygen pressures. These results are compared with theoretical predication in Fig. 6.42, where agreement is seen to be quite good. It is concluded that formation of a critical volume fraction of internal oxide constitutes a correct criterion for the transition to external scale formation. It is also observed that oxidation at low p_{O_2} provides a suitable way of inducing protective scale formation on dilute alloys. Providing these scales maintain their mechanical integrity, a low pressure preoxidation treatment can be used to provide protection against subsequent exposure to high oxygen potential gases.

We now use Eq. [6.111], with g_{BO} set at 0.3, to calculate critical alloy compositions necessary for external, rather than internal, oxide formation. Results for chromia and alumina formers are calculated using oxygen solubility data from Table 2.2, and diffusion coefficients taken from Table D2 (Appendix D). Critical values of $N_{Cr}^{(o)}$ and $N_{Al}^{(o)}$ calculated on this basis are compared in Table 6.8 with minimum values estimated from the kinetic criterion (Eq. [5.25]) for the concentration necessary to sustain external scale growth. It is seen that the concentrations necessary to avoid internal oxidation are greater than those required merely to support scale growth and should therefore be preferred under these reaction conditions.

As is also seen, fairly good agreement between prediction and experimental reality is achieved. Although the precision is much less than would be

TABLE 6.8 Calculated Minimum Solute Concentrations (Mole Fraction) for Exclusive Scale Formation Under Rhines Pack Conditions

| Alloy | Scale | T (°C) | Support scaling kinetics [5.22] | Prevent internal oxidation [6.111] | Experimental |
|--------------------|--------------------------------|-----------|---------------------------------|------------------------------------|--------------|
| Ni-Cr | Cr ₂ O ₃ | 1000 | 0.07 | 0.29 | 0.15 |
| γ-Fe-Cr | Cr ₂ O ₃ | 1000 | 0.07 | 0.16 | 0.14 |
| Ni-Al ^b | Al ₂ O ₃ | 1200 | 0.02 | 0.11 | 0.06–0.13 |
| Fe-Al ^a | Al ₂ O ₃ | 1200 | 10 ⁻⁴ | 0.15 | 0.10–0.18 |

^aData for α-Fe.^bg_{BO} set at 0.2 [89].

required for alloy design, it is concluded that the form of Eq. [6.111] may be relied upon for semiquantitative prediction. Of particular importance is the prediction that the critical alloying content required to avoid internal oxidation increases with $N_o^{(s)}$ and hence with ambient oxygen potential.

As is clear from Eq. [6.111], the competition between internal and external reaction is critically dependent on the oxidant permeability. Using the representative values of Table 6.2, it is found that the minimum value of $N_B^{(o)}$ necessary to prevent internal nitridation is two to three times higher than the value required to avoid internal oxidation in austenite. Internal carburisation is even more difficult to prevent, with the necessary values of $N_B^{(o)}$ 25–70 times higher than those required to form an oxide scale. This prediction is realistic in the sense that chromia-forming alloys are almost always found to carburise internally. In the absence of a protective oxide scale, internal carburisation of heat-resisting steels and many alloys is unavoidable. Because, moreover, the process is also very rapid, it constitutes a serious practical problem. Carburisation and related corrosion phenomena will be discussed more fully in Chapter 9.

Another reaction morphology can develop during the preferential oxidation of a single alloy component: simultaneous external scale growth and internal precipitation. Wagner [91] analysed the conditions under which this could occur by comparing the concentration product within the alloy, $N_B N_O^v$, with the solubility product of the oxide, K_{sp} . For parabolic scale growth, Eqs. [5.23]–[5.26] apply. At the alloy-scale interface, the reaction



is at equilibrium, and

$$N_{B,i} \left(N_o^{(s)} \right)^v = K_{sp} \quad [6.113]$$

The solutions to Fick's second law for oxygen diffusion from the interface into the alloy and for diffusion of B from the alloy to the interface are

$$N_o = \left(\frac{K_{sp}}{N_{B,i}} \right)^{\frac{1}{2}} \frac{erfc \left[x/2(D_o t)^{\frac{1}{2}} \right]}{erfc \left[(k_c/2D_o)^{\frac{1}{2}} \right]} \quad [6.114]$$

and

$$N_B = N_B^{(o)} - \left(N_B^{(o)} - N_{B,i} \right) \frac{erfc \left[x/2(D_{AB} t)^{\frac{1}{2}} \right]}{erfc \left[(k_c/2D_{AB})^{\frac{1}{2}} \right]} \quad [6.115]$$

These solutions are then used to evaluate the gradient in the logarithm of the concentration product at the interface ($x = x_c$)

$$\begin{aligned} \left(\frac{\partial \ln N_B N_o^v}{\partial x} \right)_{x=x_c} &= \frac{N_B^{(o)} - N_{B,i}}{N_{B,i}} \cdot \frac{1}{(\pi D_{AB} t)^{\frac{1}{2}}} \frac{\exp(-k_c/2D_{AB})}{erfc \left[(k_c/2D_{AB})^{\frac{1}{2}} \right]} \\ &\quad - \frac{v}{(\pi D_o t)^{\frac{1}{2}}} \frac{\exp(-k_c/2D_o)}{erfc \left[(k_c/2D_o)^{\frac{1}{2}} \right]} \end{aligned} \quad [6.116]$$

Noting that $D_o \gg D_{AB}$ and $k_c \leq D_{AB}$, the second term is approximated to $-v/(\pi D_o t)^{\frac{1}{2}}$. It is then found that

$$\left(\frac{\partial \ln N_B N_o^v}{\partial x} \right)_{x=x_c} = \frac{v}{(\pi D_o t)^{\frac{1}{2}}} \left[\left(\frac{\pi}{2} \right)^{\frac{1}{2}} \frac{\left(1 - N_B^{(o)} \right) (k_c D_o)^{\frac{1}{2}}}{N_{B,i} v D_{AB} \left\{ 1 - F \left[(k_c/2D_{AB})^{\frac{1}{2}} \right] \right\}} - 1 \right] \quad [6.117]$$

Here the auxiliary function $F(u)$ is as defined in Eq. [6.77].

If the right-hand side of Eq. [6.117] is negative, the concentration product decreases in the alloy from its saturation value at the interface. However, if it is positive, the alloy beneath the scale becomes supersaturated and internal oxidation results. Thus the condition for internal oxidation beneath a scale of the same oxide is

$$\left(\frac{\pi}{2} \right) \frac{1 - N_B^{(o)}}{N_{B,i}} \frac{(k_c D_o)^{\frac{1}{2}}}{v D_{AB} \left\{ 1 - F \left[(k_c/2D_{AB})^{\frac{1}{2}} \right] \right\}} > 1 \quad [6.118]$$

and the interfacial concentration is found from

$$N_{B,i} = \frac{N_B^{(o)} - F \left[(k_c/2D_{AB})^{\frac{1}{2}} \right]}{1 - F \left[(k_c/2D_{AB})^{\frac{1}{2}} \right]} \quad [6.119]$$

Alternatively, the condition for avoiding internal oxidation beneath the scale may be expressed as

$$N_B^{(o)} > \frac{R + F \left[(k_c/2D_{AB})^{\frac{1}{2}} \right]}{R + 1} \quad [6.120]$$

where $R = (\pi k_c D_o / 2)^{\frac{1}{2}} / v D_{AB}$. If k_c is small enough, then $k_c/2D_{AB} \ll 1$ and $F(k_c/2D_{AB}) \approx (\pi k_c/2D_{AB})^{\frac{1}{2}}$. If, furthermore, $D_o \gg D_{AB}$ and $k_c D_o \gg D_{AB}^2$, the condition (Eq. [6.120]) may be approximated by

$$N_B^{(o)} > \left(\frac{\pi k_c D_o}{2} \right)^{\frac{1}{2}} \cdot \frac{1}{v D_{AB}} \quad [6.121]$$

Simultaneous internal and external oxidation of B is predicted to occur when $N_B^{(o)}$ is less than the level predicted from Eq. [6.120] and greater than the value set by Eq. [6.111] for external scale formation, providing that $N_B^{(o)}$ is sufficient to support external scale growth (see Eq. [5.25]). The range of conditions permitting both internal and external oxidation of the solute metal can be rather restricted, as demonstrated by Atkinson [92] for Fe-Si alloys.

6.12 INTERNAL OXIDATION BENEATH A CORRODING ALLOY SURFACE

In many practical situations, the oxidant activity will be high, and an external scale will grow. Alloys such as Ni-Cr, Ni-Al, Fe-Cr and Fe-Al will, if sufficiently dilute, form external scales of iron or nickel-rich oxides together with internally precipitated chromium or aluminium-rich oxides. A schematic view of this reaction morphology is shown in Fig. 6.43. Interactions between the internal precipitates and iron or nickel oxides when they come into contact are considered in the next chapter. For the moment, our interest is in the effect of the receding alloy surface on the internal oxidation kinetics.

Diffusional analyses of internal oxidation in conjunction with scale growth according to parabolic kinetics have been provided by Rhines et al. [24] and Maak [93]. In this situation, $N_o^{(s)}$ denotes the dissolved oxygen concentration at the alloy-scale interface, X_i represents the distance of the internal precipitation front from the original alloy surface and X_c the position of the scale-alloy interface with respect to the original surface. In the common case $(k_p^{(i)} / 2D_o)^{\frac{1}{2}} \ll 1$ and $X_c < X_i$, then

$$X_i(X_i - X_c) = 2 \frac{N_o^{(s)} D_o}{v N_B^{(o)}} F\left(X_i/2\sqrt{D_B t}\right) t \quad [6.122]$$

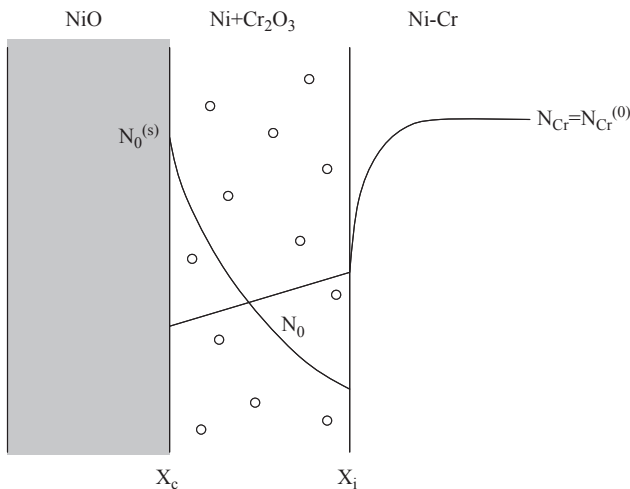


FIGURE 6.43 Oxidation of a dilute Ni-Cr alloy at high p_{O_2} .

where the function $F(u)$ is as defined in Eq. [6.78]. When both X_c and D_B are small, Eq. [6.122] yields Eq. [6.11].

Experimental verification of Eq. [6.122] has not been completely successful [9]. Permeability values deduced from internal oxidation kinetics under an external scale were apparently smaller than those determined from exclusively internal reactions. In view of the microstructural complexity of the scale-alloy interface (Fig. 6.43), it seems quite likely that local scale separation could occur from time to time, as a result of reduced oxide plasticity. In this case, the boundary value oxygen activity, and hence $N_0^{(s)}$, would vary with time, and Eq. [6.122] would no longer apply.

6.13 VOLUME EXPANSION IN THE INTERNAL PRECIPITATION ZONE

The precipitation of internal oxides is almost always accompanied by a volume expansion. As is seen from the molar volumes listed in Table 6.9, the expansions are large. The effect of internal oxide precipitation on the molar volume of the internal oxidation zone can be calculated for a binary alloy Ni-B as

$$V_T = V_{\text{Ni}} \left(1 - N_B^{(o)} \right) + N_B^{(o)} V_{\text{BO}_v} \quad [6.123]$$

where it is assumed that no solute element enrichment or depletion occurs. The volume increase ratio $\Delta V/V_{\text{Alloy}} = (V_T - V_{\text{Alloy}})/V_{\text{Alloy}}$ is then calculated for various solute concentrations, leading to the results shown in Table 6.9. Similar calculations for nitridation and carburisation of chromium show that

TABLE 6.9 Molar Volumes of Internal Oxides: Alloy Expansion on Internal Oxidation of Ni-Base Alloys

| | | Alloy $\Delta V/V$ | | |
|--|------|--------------------|------|------|
| V_i (cm ³) | | $N_B^{(0)} = 0.01$ | 0.05 | 0.10 |
| SiO ₂ ^a | 25.8 | 0.026 | 0.13 | 0.26 |
| α -Al ₂ O ₃ | 25.6 | 0.008 | 0.04 | 0.08 |
| Cr ₂ O ₃ | 29.2 | 0.011 | 0.05 | 0.11 |

^a β -cristobalite.

resulting expansions are less, principally because of the higher densities of Cr₂N and the chromium carbides, all of which are interstitial compounds.

In the case of internal oxidation, the enormous volume increase generates stresses which must be relieved. Shida et al. [33,43] suggested stress relief mechanisms of grain boundary sliding and extrusion of internal oxide-free metal adjacent to grain boundaries, in the case of intergranular oxidation at low temperature. On the other hand, internally oxidised Ni-Cr alloys were thought [36] to be able to accommodate stress by metal flow within the grains. In fact, outward transport of the more noble metal was first reported by Darken [94] in a study of Ag-Al alloy oxidation. Mackert et al. [95] found nodules of palladium and silver on the external surface of internally oxidised Pd-Ag-Sn-In alloys and proposed that Pd and Ag diffused via the Nabarro-Herring mechanism. Guruswamy et al. [96] observed silver nodules on the surface of internally oxidised Ag-In alloys and concluded that dislocation pipe diffusion was the mechanism of silver transport. An example of outward metal displacement during internal oxidation of Ni-Cr-Al is shown in Fig. 6.8.

Yi et al. [36] demonstrated that in the case of Ni-Al-Si internal oxidation, the volume of metal accumulated outside the precipitation zone was close to the equivalent of the volume increase calculated for silicon and aluminium oxidation. This result is shown in Fig. 6.44 and confirms that the driving force for outward nickel displacement is the volume increase within the precipitation zone. The mechanism whereby the nickel moves is obviously of interest.

Yi et al. [34] proposed that the mechanism was one of Nabarro-Herring creep [97]. In the case of internal oxidation, the volume expansion at the internal oxidation front causes compressive stress and a reduction in vacancy concentration. Thus a vacancy gradient is established between the free alloy surface, where the equilibrium concentration N_v prevails, and a much reduced concentration at the reaction front. Assuming a linear gradient, we can write

$$J_{Ni} = -J_V = \frac{D_V \Delta N_V}{X_i V_{Ni}} \quad [6.124]$$

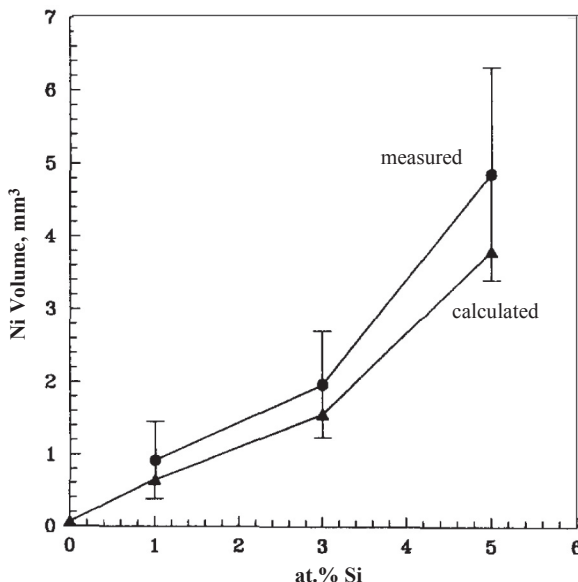


FIGURE 6.44 Comparison of volume of Ni transported outward with volume increase calculated for internal oxidation of Al and Si in Ni-Al-Si. Reprinted from with permission from H.C. Yi, S.W. Guan, W.W. Smeltzer, A. Petric, *Acta Met. Mat.* 42 (1994) 981, Elsevier.

where D_V is the vacancy diffusion coefficient. To conserve mass, this flux must equal the rate at which nickel is displaced by newly precipitated oxide

$$J_{\text{Ni}} = \frac{N_B^{(o)}(V_{\text{BO}} - V_B)}{V_{\text{Ni}}} \cdot \frac{1}{V_{\text{Ni}}} \frac{dX_i}{dt} \quad [6.125]$$

where the amount of nickel displaced has been calculated from the volume of new materials divided by the nickel molar volume. Equating Eqs [6.124] and [6.125] and integrating, we find $X_i^2 = 2k_p^{(i)}t$ with

$$k_p^{(i)} = \frac{D_V \Delta N_V V_{\text{Ni}}}{N_B^{(o)}(V_{\text{BO}} - V_B)} \quad [6.126]$$

If the further approximation $N_V(x = X_i) \approx 0$ is made, then $\Delta N_V = N_V$. Recalling that $D_{\text{Ni}} \approx D_V N_V$, we obtain

$$k_p^{(i)} = \frac{D_{\text{Ni}} V_{\text{Ni}}}{N_B^{(o)}(V_{\text{BO}} - V_B)} \quad [6.127]$$

Values of $k_p^{(i)}$ predicted from Eq. [6.127] are compared with experimental measurements for a Ni-4Al alloy in Fig. 6.45, where agreement is seen to be good. Thus internal oxidation is, in this case, controlled by outward diffusion of nickel, although it is driven by inward oxygen diffusion. It is likely that the

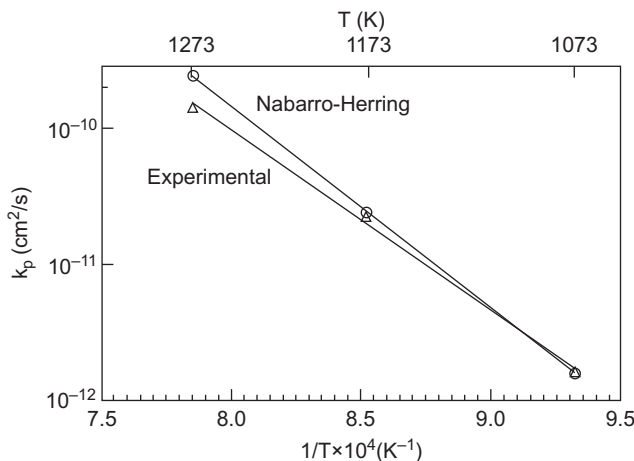


FIGURE 6.45 Comparison of experimentally measured internal oxidation rates with predictions of Nabarro–Herring creep mechanism. Reprinted from with permission from H.C. Yi, S.W. Guan, W.W. Smeltzer, A. Petric, *Acta Met. Mat.* 42 (1994) 981, Elsevier.

rapid oxygen diffusion associated with the fine precipitate platelets was a factor contributing to this result.

The Nabarro–Herring model was found by Yi et al. [34] to be inapplicable to Ni-4Al-xSi alloys with $x = 1$ or 5 wt pct. Instead of decreasing with increasing $N_{Si}^{(o)}$ as predicted by Eq. [6.127], the rate increased. Although the magnitude of the rate constant was satisfactorily accounted for by dislocation pipe diffusion of nickel, the variation of $k_p^{(i)}$ with $N_{Si}^{(o)}$ was not. It is possible that increasing silicon levels led to a greater multiplicity of precipitate-matrix interfaces and consequently higher effective D_o values. If dislocation pipe diffusion is sufficiently rapid, the process does not contribute to rate control, and internal oxidation kinetics are described using an expression like Eq. [6.35] for the ternary alloy:

$$N_o^{(s)} D_o = a + b(N_{Al}^{(o)} + N_{Si}^{(o)}) \quad [6.128]$$

A more detailed study of precipitate morphologies is required.

The swelling effect caused by internal oxidation is not universally observed to cause metal ejection. For example, internal precipitation of Cr_2O_3 and MCr_2O_4 in Fe-Cr (Figs 6.1 and 6.2) or Ni-Cr [36] does not lead to external iron or nickel accumulation. The volume changes are nonetheless large (Table 6.9), and significant deformation must occur. It is possible that outward movement of nickel simply carries with it the embedded chromium-rich particles. The latter are large and spheroidal and drift with the moving nickel lattice. Alumina, however, precipitates as rods and platelets normal to the alloy surface, ie, parallel to the direction of nickel movement. In such a configuration, it

seems possible that nickel can transport past the fixed alumina precipitates, ‘extruding’ to the outer surface.

Even when this favourable morphology develops, nickel displacement has been found to be suppressed if an external NiO scale grows during internal Al_2O_3 precipitation within a binary Ni-Al alloy oxidised at $p_{\text{O}_2} = 1 \text{ atm}$ [72]. The suggested reason [33,39,71] is that growth of an external scale by outward cation diffusion leads to metal vacancies being injected into the alloy at the scale-alloy interface. These then diffuse inwards, permitting more rapid outward nickel movement. Put more simply, consumption of metal at the scale-alloy interface provides the space needed to accommodate the internally precipitated oxide.

A similar situation arises during in situ oxidation of primary carbides (Fig. 6.16) beneath a growing Cr_2O_3 scale [39]. If the carbide oxidation is described by Eq. [6.42], then the weight change corresponding to oxygen consumption is given by

$$\frac{(\Delta W_i/A)^2}{2t} = k^{(i)} = \left(\frac{k_p^{(i)} f_{\text{Cr}_{23}\text{C}_6}}{V_{\text{CrC}_{0.261}}} \right)^2 576 \quad [6.129]$$

where the mass conversion number 576 is computed on the assumption that no carbon is lost from the alloy. The volume increase due to carbide oxidation, normalised to the alloy surface area, is then given by

$$\frac{(\Delta V_i/A)^2}{2t} = k_v^{(i)} = k^{(i)} \frac{(V_{\text{CrO}_{1.5}} - V_{\text{CrC}_{0.261}})}{24} \quad [6.130]$$

The rate of the process was measured as $k_p^{(i)} = 2.9 \times 10^{-11} \text{ cm}^2 \text{ s}^{-1}$, corresponding to a volume expansion accumulation rate of $k_v^{(i)} = 3 \times 10^{-15} \text{ cm}^2 \text{ s}^{-1}$. This is to be compared with the volume consumption rate corresponding to external scale growth, ΔV^{ex} . Approximating the scale as pure Cr_2O_3 and assuming a fixed alloy-scale interface, one finds

$$\frac{(\Delta V_{\text{ex}}/A)^2}{2t} = k_v^{(\text{ex})} = \left(\frac{V_{\text{Cr}}}{k_w} \right)^2 k_w \quad [6.131]$$

where k_w is the parabolic weight gain rate constant for scale growth. The measured value of $k_w = 8 \times 10^{-12} \text{ g}^2 \text{ cm}^{-4} \text{ s}^{-1}$ leads to an estimate of $k_v^{(\text{ex})} = 6.5 \times 10^{-13} \text{ cm}^2 \text{ s}^{-1}$. The volume made available, if external scaling causes injection of vacancies at the alloy surface, is very much larger than the volume required to accommodate the expansion due to interdendritic carbide oxidation.

Intragranular precipitation of Al_2O_3 rods within Al-bearing heat-resistant steels takes place according to parabolic kinetics [39,98] together with external chromium-rich oxide scale growth at high p_{O_2} values. No oxide-free surface region of metal develops (Fig. 6.46). This is quite unlike the extensive metal ejection observed in the absence of scaling on a dilute alloy (Fig. 6.8).

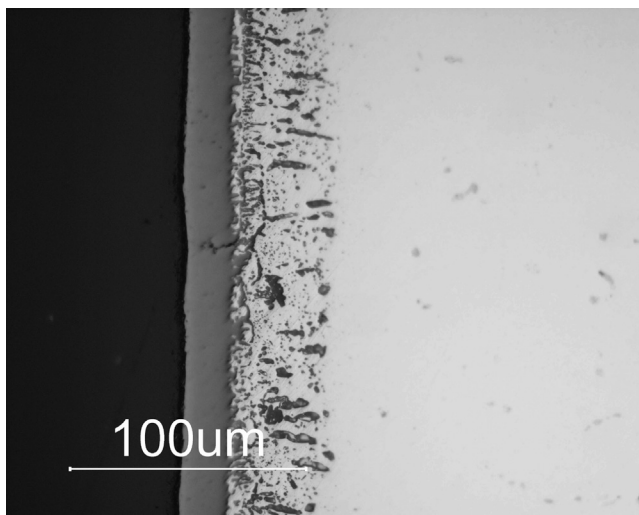


FIGURE 6.46 Internal aluminium oxidation and external chromia scale growth on Ni-25Cr-10Fe-2.5Al cast heat-resisting alloy ($T = 1250^\circ\text{C}$, $p_{\text{O}_2} = 4 \times 10^{-14}$ atm).

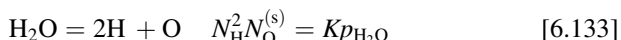
Measurement of internal penetration and scale thickening rates allowed calculation of the volume expansion rate $k_v^{(\text{i})} = 6.3 \times 10^{-14} \text{ cm}^2 \text{ s}^{-1}$ and the rate of free volume generation by vacancy injection $k_v^{(\text{ex})} = 1 \times 10^{-12} \text{ cm}^2 \text{ s}^{-1}$ at 1000°C and $p_{\text{O}_2} = 0.2$ atm. In this instance the internal expansion corresponds to the reaction



Again, the volume potentially made available by the scaling process is substantially larger than that needed to accommodate the expansion due to internal oxidation, and the absence of visible metal displacement is thereby explained.

6.14 EFFECTS OF WATER VAPOUR ON INTERNAL OXIDATION

The presence of H_2O in the gas atmospheres has been found to accelerate the degradation of chromia forming alloys at high temperatures. One explanation proposed [99,100] for this effect is that hydrogen increases the amount of internal oxidation of alloy chromium, resulting in a more rapid onset of breakaway oxidation. If water vapour increases $k_p^{(\text{i})}$ for an alloy, an increase in oxygen permeability, $N_{\text{O}}^{(\text{s})}D_{\text{O}}$, is implied. Direct dissolution of water molecules



was suggested [100] to be accompanied by rapid diffusion of solute hydrogen away from the alloy surface, and a lower value of N_{H} . A consequent increase

in the value of $N_O^{(s)}$ was thought to explain an increase in internal oxidation rate. This mechanism seems unlikely to apply in the case where an external scale is formed, and $N_O^{(s)}$ is controlled by the scale oxide-alloy equilibrium. However, it might play a role when a bare alloy surface is in direct contact with water vapour. Another possibility is that of thermodynamic interaction between the different interstitial solutes, \underline{H} and \underline{O} , leading to an enhanced value of D_O .

These possibilities have been tested by internally oxidising dilute Ni-Cr alloys in H_2/H_2O , CO_2/CO and Ni/NiO Rhines packs, setting the oxygen partial pressures in the mixed gases equal to that of the Ni/NiO equilibrium [101]. Internal oxidation occurred in all cases, according to parabolic kinetics, indicating a diffusion-controlled process. Typical data for internal oxidation at 1000°C are shown in Fig. 6.47. Oxygen permeabilities deduced from Wagner's diffusion model showed that any variation between the H_2/H_2O and CO_2/CO reactions is within the range of measurement error ($\leq 10\%$). However, oxygen permeability was slightly higher in the Rhines pack environment, a result attributed to the formation of more needle-like internal precipitates and faster diffusion along precipitate-matrix interfaces. It is concluded on this basis that oxygen permeability in nickel is not increased by the presence of hydrogen or carbon.

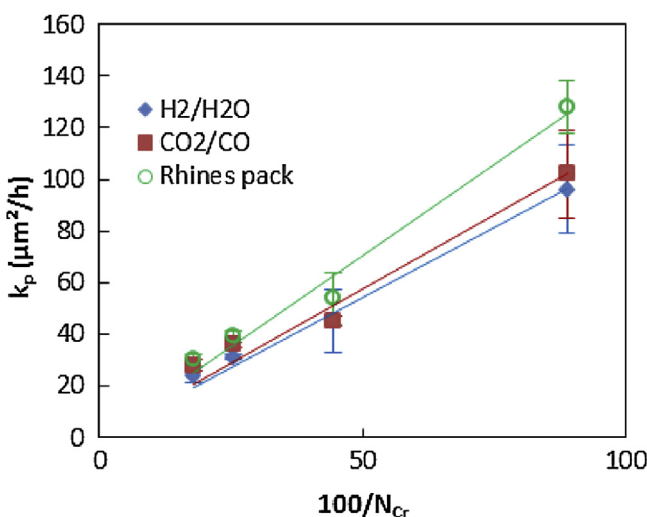


FIGURE 6.47 Internal oxidation rates of Ni-Cr alloys as a function of composition, measured at 1000°C in different environments, all corresponding to the Ni/NiO equilibrium p_{O_2} value. Data from P. Guo, J. Zhang, D.J. Young, C.H. Konrad, *Oxid. Met.* 83 (2015) 223.

Using the Rhines pack method, Ani et al. [102] and Setiawan et al. [103] compared oxygen permeabilities of binary Fe-Cr alloys in wet and dry packs and found slightly increased values in the presence of water vapour. At 800°C, the value of $N_O^{(s)}D_O$ deduced from internal oxidation depths was found to increase by a factor of 1.4 in the presence of water vapour, with $p_{H_2O} \approx 100\text{--}300$ Pa. They attributed this increase to the change of precipitate morphology from fine grained in dry Rhines packs to relatively large and acicular in wet packs. Diffusion along precipitate-matrix interfaces in the latter case was thought to accelerate overall oxygen mass transport. According to Eq. [6.111], an increase in $N_O^{(s)}D_O$ by a factor of 1.4 should lead to an increase of about 20% in the critical concentration of chromium required to form an external scale rather than internal precipitates. The experimentally observed increase was however about 50%, from 8 to 12 wt%, suggesting that precipitate shape changes may have additional effects.

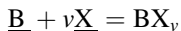
A recent study [104,105] of internal oxidation at 1000°C of dilute Ni-Cr-Al alloys in dry air and air + 30% water vapour characterised the development of a duplex internal precipitation zone of NiAl_2O_4 and Al_2O_3 beneath a scale of NiO . Comparison of internal oxidation rates in wet and dry gases showed that water vapour caused a decrease in $N_O^{(s)}D_O$ by about 25%. This is qualitatively in agreement with the results of Fig. 6.47 but the opposite of the permeability enhancement discussed above for Fe-Cr alloys. Of course, the metal matrices in the two cases are different: bcc iron on the one hand, and fcc nickel on the other.

A common feature of these investigations is the observation that the presence of water vapour changes the oxide precipitate morphology, although oxide volume fraction remains unchanged. In dry gases, precipitates are relatively fine, whereas in wet gas reactions, oxide particles are coarser and less numerous. As pointed out by Zhao and Gleeson [104,105], the consequently greater spacing between particles means that even more additional oxide is required to form a continuous layer. In effect, the critical precipitate volume fraction required for the transition from internal to external oxide formation, g_{BO} in Eq. [6.111], is increased by the presence of water vapour. The critical questions therefore concern the ways in which the competition between precipitate nucleation and growth is affected by the presence of hydrogen. Answers are not yet available.

6.15 SUCCESS OF INTERNAL OXIDATION THEORY

Internal precipitation in alloys resulting from reactions with external oxidants is a highly destructive process, frequently leading to alloy failure when it occurs. As we have seen in this chapter, these reactions can develop a diversity of morphologies, at rates which vary over orders of magnitude with oxidant

identity and the alloy composition and phase constitution. However, the reactions all involve simple, solid-state precipitation processes:



where X is a generic oxidising solute. Consequently, local equilibrium is closely approached at intermediate and high temperatures, and solubility product calculations work well. For this reason, the diffusion path description applies and diffusion-controlled parabolic kinetics result.

In the case of the fast-diffusing oxidants carbon and nitrogen, the diffusion path for the system A–B–X can usually be defined on the basis $D_X \gg D_B$ simply as a straight line from the X-corner of the ternary to the AB alloy composition. This approach correctly describes the sequence of precipitate phase constitutions, the variation in composition of mixed carbides such as $(\text{Cr},\text{Fe})_7\text{C}_3$ and the change in volume fraction with depth of these low-stability compounds. Even for the slower diffusing oxygen, this approach is useful. Prediction from these simplified diffusion paths is successful for multiple oxidants and multicomponent alloys, but inaccurate when fast diffusing alloy solutes such as silicon and aluminium are involved (Fig. 6.46).

Rather simple diffusion theory usually succeeds in predicting parabolic rate constants very well for binary alloys, providing that both D_X and $N_X^{(s)}$ are known. The measured permeabilities of carbon and oxygen in austenite and ferrite provide good order of magnitude predictions of the relative rates of the various internal precipitation reactions, with internal carburisation being almost three orders of magnitude faster than oxidation. Unfortunately, data for nitridation are scant. In the absence of such data, internal oxidation kinetic measurements can be used to evaluate permeabilities.

The kinetic theory is particularly valuable in predicting the increase in rate with oxidant solubility and diffusivity, and hence with a_X and temperature. It also successfully predicts the decrease in rate with increasing $N_B^{(o)}$ for cases of dispersed precipitates. However, the theory has mixed success in describing the growth of multiple precipitation zones. The total depth of attack is reasonably well-predicted, but quantitative calculation of the individual precipitate zones is not yet possible. From a practical point of view, this may be unimportant to the prediction of alloy failure. However, if the reaction is to be used as a method of fabricating nanostructures, this deficiency needs to be addressed.

The classical theories of internal oxidation all assume uniform distributions of precipitates. This insistence upon a strict chemical stoichiometry ignores the effects of low precipitate K_{sp} values, microstructure and alloy phase transformations and can lead to error. As we have seen, the competition between precipitate nucleation and growth can have important effects. It alters size distributions, and therefore penetration depths. In the extreme, it can produce cellular precipitation morphologies which are associated with rapid

boundary diffusion and accelerated reaction. The alloy phase transformations or crystallographic reorientations accompanying this process have been well-characterised in a number of cases, but a satisfactory description of fibrous alumina precipitate growth has not yet been arrived at.

From an alloy design (or selection) point of view, the most important thing about internal oxidation is avoiding it. The diffusion-based theory provides a method for predicting how much alloy solute metal is required to ensure external scale growth rather than internal precipitation of the preferentially formed oxide. Its predictions are approximately correct, and a sound basis for alloy design is potentially available. However, for this method to be a useful design tool, we require greater accuracy. To achieve this, a much better knowledge of the solute interactions which determine thermodynamic activities and diffusivities of oxidant and alloy components is required.

REFERENCES

- [1] R.C. John, in: Corrosion 96, NACE, Houston, TX, 1996. Paper 171.
- [2] C.S. Smith, *Min. Met.* 11 (1930) 213.
- [3] C.S. Smith, *J. Inst. Met.* 46 (1931) 49.
- [4] F.N. Rhines, *Trans. AIME* 137 (1940) 246.
- [5] F.N. Rhines, A.H. Grobe, *Trans. AIME* 147 (1942) 318.
- [6] J.L. Meijering, M.J. Druyvesten, *Philips Res. Rept.* 2 (1947) 81.
- [7] J.L. Meijering, M.J. Druyvesten, *Philips Res. Rept.* 2 (1947) 260.
- [8] C. Wagner, *Z. Elektrochem.* 63 (1959) 772.
- [9] R.A. Rapp, *Corrosion* 21 (1965) 382.
- [10] O. Ahmed, D.J. Young, in: M.J. McNallan, E.J. Opila, T. Maruyama, T. Narita (Eds.), *High Temperature Corrosion and Materials Chemistry II*, The Electrochemical Society, Inc., Pennington, NJ, 2000, p. 77.
- [11] J.L. Meijering, in: H. Herman (Ed.), *Advances in Materials Research*, Wiley-Interscience, New York, 1971, p. 1.
- [12] J.H. Swisher, in: *Oxidation of Metals and Alloys*, ASM, Metals Park, OH, 1971, p. 235.
- [13] J.L. Meijering, *Acta Met.* 3 (1955) 157.
- [14] W. Eichenaur, G. Müller, *Z. Metallk.* 53 (321) (1962) 700.
- [15] V. Gottardi, *Metal. Ital.* 44 (1952) 424.
- [16] G. Böhm, M. Kahlweit, *Acta Met.* 12 (1964) 641.
- [17] E. Raub, W. Plate, *Metall* 10 (1956) 620.
- [18] H. Spengler, *Metall* 17 (1963) 710.
- [19] G. Zwingmann, *Metall* 17 (1963) 796.
- [20] J.E. Verfuth, R.A. Rapp, *Trans. AIME* 230 (1964) 1310.
- [21] D.P. Whittle, Y. Shida, G.C. Wood, F.H. Stott, B.D. Bastow, *Phil. Mag. A* 46 (1982) 931.
- [22] J.-W. Park, C.J. Altstetter, *Met. Trans. A* 18A (1987) 43.
- [23] D.J. Young, O. Ahmed, *Mater. Sci. Forum* 369–372 (2001) 93.
- [24] F.N. Rhines, W.A. Johnson, W.A. Anderson, *Trans. AIME* 147 (1942) 205.
- [25] H.J. Grabke, E.M. Peterson, *Scripta Met.* 12 (1978) 1111.
- [26] H.A. Wriedt, O.D. Gonzalez, *Trans. AIME* 221 (1961) 532.
- [27] S.K. Bose, H.J. Grabke, *Z. Metallk.* 69 (1978) 8.

- [28] T. Wada, H. Wada, J.F. Elliott, J. Chipman, *Met. Trans.* 2 (1971) 2199.
- [29] F.H. Stott, G.C. Wood, D.P. Whittle, B.D. Bastow, Y. Shida, A. Martinez-Villafane, *Solid State Ionics* 12 (1984) 365.
- [30] S.F. Ford, Ph.D. Thesis, University Of New South Wales, 2004.
- [31] J.S. Wolf, E.B. Evans, *Corrosion* 18 (1962) 129.
- [32] S. Goto, S. Koda, *J. Jpn. Inst. Met.* 32 (1968) 334.
- [33] Y. Shida, F.H. Stott, B.D. Bastow, D.P. Whittle, G.C. Wood, *Oxid. Met.* 18 (1982) 93.
- [34] H.C. Yi, S.W. Guan, W.W. Smeltzer, A. Petric, *Acta Met. Mat.* 42 (1994) 981.
- [35] S. Goto, K. Nomaki, S. Koda, *J. Jpn. Inst. Met.* 31 (1967) 600.
- [36] G.C. Wood, F.H. Stott, D.P. Whittle, Y. Shida, B.D. Bastow, *Corros. Sci.* 23 (1983) 9.
- [37] Y. Miyoshi, S. Kado, *J. Jpn. Inst. Met.* 31 (1967) 481.
- [38] P. Becker, M. Panasko, D.J. Young, *Oxid. Met.* 64 (2005) 281.
- [39] N. Belen, P. Tomaszewicz, D.J. Young, *Oxid. Met.* 22 (1984) 227.
- [40] F.S. Pettit, *Trans. Met. Soc. (AIME)* 239 (1967) 1296.
- [41] H. Hindam, W.W. Smeltzer, *J. Electrochem. Soc.* 127 (1980) 1622.
- [42] H. Hindam, D.P. Whittle, *J. Mater. Sci.* 18 (1983) 1389.
- [43] F.H. Stott, Y. Shida, D.P. Whittle, G.C. Wood, B.D. Bastow, *Oxid. Met.* 18 (1982) 127.
- [44] A. Martinez-Villafane, F.H. Stott, J.G. Chacon-Nova, G.C. Wood, *Oxid. Met.* 57 (2002) 267.
- [45] G.J. Tatlock, R.W. Devenish, J.S. Punni, in: M.J. Bennett, G.W. Lorimer (Eds.), *Microscopy of Oxidation*, Institute of Metals, London, 1991, p. 176.
- [46] D.J. Young, M.L. Burg, P.R. Munroe, *Mater. Sci. Forum* 461–4 (2004) 21.
- [47] O. Kubaschewski, C.B. Alcock, P.J. Spencer, *Materials Thermochemistry*, sixth ed., Pergamon Press, Oxford, 1993.
- [48] T.R. Rosenqvist, *Principles of Extractive Metallurgy*, McGraw-Hill, New York, 1974.
- [49] G.C. Savva, G.C. Weatherly, J.S. Kirkaldy, *Mat. Trans. A* 27A (1996) 1611.
- [50] J.S. Kirkaldy, *Canad. Met. Q.* 8 (1969) 35.
- [51] E.K. Ohriner, J.F. Morral, *Scripta Met.* 13 (1979) 7.
- [52] M. Udyavar, D.J. Young, *Corros. Sci.* 42 (2000) 861.
- [53] S.I. Ford, P.R. Munroe, D.J. Young, *Micron* 32 (2001) 817.
- [54] C. Wagner, *Corros. Sci.* 8 (1968) 889.
- [55] M. Kahlweit, *Progr. Chem. Solid State* 2 (1965) 134.
- [56] P. Bolsaitis, M. Kahlweit, *Acta Met.* 15 (1967) 765.
- [57] F. Gesmundo, P. Castello, F. Viani, C. Roos, *Oxid. Met.* 49 (1998) 237.
- [58] D.J. Young, J.S. Kirkaldy, W.W. Smeltzer, *J. Electrochem. Soc.* 123 (1976) 1758.
- [59] R.A. Rapp, D.F. Frank, J.V. Armitage, *Acta Met.* 12 (1964) 505.
- [60] J. Megasur, G.H. Meier, *Met. Trans. A* 7A (1976) 1133.
- [61] D.L. Douglass, *J. Met.* 43 (1991) 74.
- [62] J.J. Barned, G.Y. Lai, in: V. Srinivasan, K. Vedula (Eds.), *Corrosion and Particle Erosion at High Temperatures*, TMS, Warrendale, PA, 1989, p. 617.
- [63] K. Tjokro, D.J. Young, *Oxid. Met.* 44 (1995) 453.
- [64] K.P. Bunin, *Izv. Chern. Metall.* 2 (1973) 123.
- [65] V.I. Movchan, *Izv. Chern. Metall.* 8 (1979) 92.
- [66] S.I. Ford, P.R. Munroe, D.J. Young, *Mater. High Temp.* 17 (2000) 279.
- [67] J.W. Cahn, *Acta Met.* 7 (1959) 18.
- [68] D. Turnbull, *Acta Met.* 3 (1955) 55.
- [69] D.B. Williams, E.P. Butler, *Int. Met. Rev.* 3 (1981) 153.

- [70] S.I. Ford, P.R. Munroe, D.J. Young, in: P.F. Tortorelli, I.G. Wright, P.Y. Hou (Eds.), John Stringer Symposium, ASM International, Materials Park OH, 2003, p. 77.
- [71] Y. Niu, F. Gesmundo, *Oxid. Met.* 60 (2003) 371.
- [72] H.C. Yi, S.-Q. Shi, W.W. Smeltzer, A. Petric, *Oxid. Met.* 43 (1995) 115.
- [73] J.A. Colwell, R.A. Rapp, *Met. Trans. A* 17A (1986) 1065.
- [74] C.J. Spengler, R. Viswanathan, *Met. Trans.* 3 (1972) 161.
- [75] D.J. Young, S. Watson, *Oxid. Met.* 44 (1995) 239.
- [76] F. Gesmundo, Y. Niu, *Oxid. Met.* 51 (1999) 129.
- [77] B.E. Hopkinson, H.R. Copson, *Corrosion* 16 (1960) 608.
- [78] H.R. Copson, F.S. Lang, *Corrosion* 15 (1959) 194.
- [79] W. Betteridge, *The Nimonic Alloys*, E. Arnold, London, 1959.
- [80] M. Hänsel, C.A. Boddington, D.J. Young, *Corros. Sci.* 45 (2003) 967.
- [81] S. Han, D.J. Young, *Oxid. Met.* 55 (2001) 225.
- [82] S. Ford, D.J. Young, D. McGrouther, P.R. Munroe, *Mater. High Temp.* 22 (2005) 351.
- [83] F. Gesmundo, Y. Niu, *Oxid. Met.* 60 (2003) 347.
- [84] C.B. Alcock, F.D. Richardson, *Acta Met.* 6 (1958) 385.
- [85] J.-B. Park, C. Altstetter, *Acta Met.* 34 (1986) 2217.
- [86] S.W. Guan, W.W. Smeltzer, *Oxid. Met.* 42 (1994) 375.
- [87] U. Krupp, H.-J. Christ, *Oxid. Met.* 52 (1999) 277.
- [88] L.S. Darken, *Trans. AIME* 150 (1942) 157.
- [89] R.A. Rapp, *Acta Met.* 9 (1961) 730.
- [90] J.A. Nesbitt, *J. Electrochemical. Soc.* 136 (1989) 1511.
- [91] C. Wagner, *Corros. Sci.* 8 (1968) 889.
- [92] A. Atkinson, *Corros. Sci.* 22 (1982) 87.
- [93] F. Maak, *Z. Metallk.* 52 (1961) 538.
- [94] L.S. Darken, *Trans. AIME* 54 (1961) 600.
- [95] J.R. Mackert, R.D. Ringle, C.W. Fairhurst, *J. Dent. Res.* 62 (1983) 1229.
- [96] S. Guruswamy, S.M. Park, J.P. Hirth, R.A. Rapp, *Oxid. Met.* 26 (1986) 77.
- [97] C. Herring, *J. Appl. Phys.* 21 (1950) 437.
- [98] P. Becker, PhD Thesis, University of New South Wales, 2004.
- [99] E. Essuman, G.H. Meier, J. Zurek, M. Hansel, L. Singheiser, W.J. Quadakkers, *Scripta Mater.* 57 (2007) 845.
- [100] E. Essuman, G.H. Meier, J. Zurek, M. Hansel, W.J. Quadakkers, *Oxid. Met.* 69 (2008) 143.
- [101] P. Guo, J. Zhang, D.J. Young, C.H. Konrad, *Oxid. Met.* 83 (2015) 223.
- [102] M.H.B. Ani, T. Kodama, M. Ueda, K. Kawamura, T. Maruyama, *Mater. Trans.* 50 (2009) 2656.
- [103] A.R. Setiawan, M.H.B. Ani, M. Ueda, K. Kawamura, T. Maruyama, *ISIJ Int.* 50 (2010) 259.
- [104] W. Zhao, B. Gleeson, *Oxid. Met.* 79 (2013) 613.
- [105] W. Zhao, B. Gleeson, *Oxid. Met.* 83 (2015) 607.